

# Plasma Moments in the environment of Mars

## Mars Express ASPERA-3 Observations

M. Fränz · E. Dubinin · E. Roussos · J. Woch ·  
J.D. Winningham · R. Frahm · A. Fedorov ·  
A.J. Coates · S. Barabash · R. Lundin

Received: date / Accepted: date

**Abstract** We present the first electron and ion moment maps (density, velocity and temperature) of the martian plasma environment, using data from the ELS and IMA sensors of the ASPERA-3 experiment onboard Mars Express. Moments are calculated by integration and by Gaussian fits to the phase space distribution. The methods of calculation and the calibration parameters relevant for the calculation are described in detail in the first part of the paper. The estimation of ionospheric electron densities assumes that the thermal electron temperature can be determined by the instrument - despite a cut-off by a negative spacecraft potential. The spacecraft potential is estimated by the location of photoelectron peaks in the energy spectrum. For the magnetosheath we separate the low energy part of the electron spectrum - presumably spacecraft photo electrons and the high energy part. For ions, we present maps for solar wind protons and alpha particles. Protons with energies below 500eV which may play an important role in the ionosphere are not measured by the instrument. As well the low speed solar wind protons are not sampled very well. The maps reveal all the boundaries of the Mars-solar wind interaction and give a good qualitative description of the plasma behavior at the different interaction regions.

**Keywords** Mars · magnetosphere · plasma moments

---

M. Fränz · E. Dubinin · E. Roussos · J. Woch  
MPI für Sonnensystemforschung, 37191 Katlenburg-Lindau, Germany  
Tel.: +49-5556-979441, Fax: +49-5556-979240, E-mail: fraenz@mps.mpg.de

J. D. Winningham · R. Frahm  
Southwest Research Institute, San Antonio, TX 78228-0510, USA

A.J. Coates  
Mullard Space Science Laboratory, University College London, Surrey RH5 6NT, UK

A. Fedorov  
Centre d'Etude Spatiale des Rayonnements, BP-4346, F-31028 Toulouse, France

S. Barabash · R. Lundin  
Swedish Institute of Space Physics, Box 812, S-98 128, Kiruna, Sweden

---

## Contents

1	Introduction	2
2	Instrumentation	3
3	Plasma Moment Calculation from Particle Counters	3
3.1	Moments by integration	4
3.2	Moments by fitting	6
4	Electron moments from ASPERA-3 ELS	8
4.1	Discussion of ELS spectra and moments	10
5	Ion moments from ASPERA-3 IMA	13
5.1	Noise Reduction	16
5.2	Mass Ring Efficiencies	16
5.3	Anode and Theta Efficiencies	17
5.4	Species Separation	19
5.5	Resulting IMA moments	21
6	Plasma moment statistics in the environment of Mars	27
6.1	Spatial binning	27
6.2	Electron densities	31
6.3	Electron temperatures	33
6.4	Proton densities	33
6.5	Ion Velocities	33
6.6	Proton Temperatures	36
6.7	Alpha densities	36
7	Summary and Conclusions	36

## 1 Introduction

The plasma environment of Mars has been keeping many secrets up to the present day (see the reviews by *Nagy et al.* [15] and *Luhmann and Brace* [11]). While the average location of the main plasma boundaries (bow shock and magnetic pile-up boundary, MPB) have been studied in depth using the Mars Global Surveyor (MGS) magnetometer instrument [14, 19] the fundamental question of how the pressure balance between ionosphere of Mars and the solar wind is achieved remains unsolved. The reason for this has been the insufficient instrumentation for plasma investigations on previous missions. In this paper we follow the terminology of [15] by calling the region between bow shock and MPB magnetosheath. With the spatial resolution used in this paper we cannot identify an ionopause (if it is different from the MPB) and call the region inside the MPB ionosphere. Only during the Viking lander missions altitude profiles of the ionospheric plasma densities and temperatures have been obtained. The Phobos-2 mission, which had the ASPERA-1 plasma instrument onboard, had too short of a lifetime to deliver enough statistics on the plasma parameters [12]. The electron-reflectometer on MGS has been giving excellent results on the morphology of the ionosphere [3] but it was so far not possible to extract plasma densities, velocities and temperatures from the data because of instrumental restrictions. With two years of operation of the ASPERA-3 instrument on board the Mars Express spacecraft it is for the first time possible to determine large scale statistics of plasma moments in the environment of Mars. In this paper we present and discuss data obtained by the ELS electron sensor and IMA ion sensor of the ASPERA-3 experiment between February 2004 and January 2006. Unfortunately there are again severe instrumental restrictions for the analysis: 1) Electron spectra are strongly influenced by the charging of the spacecraft with respect to the local plasma environment (*spacecraft potential*). Fortunately the energy resolution of the ELS sensor is good enough to resolve peaks in the spectrum caused by ionospheric photo electrons. These peaks allow an estimation of the spacecraft potential in the ionosphere. Outside of the ionosphere we can only calculate

electron moments by assuming different levels of (positive) spacecraft potential. 2) the IMA sensor does not measure protons below a threshold of about 500eV (depending on instrument mode), so that we cannot give an estimate of proton moments in the ionosphere. For heavier ions the separation of  $O^+$ ,  $O_2^+$  and  $CO_2^+$  is rather difficult [4], thus we will discuss moments of heavy ions in a later paper and present only proton and alpha particle moments in this paper.

## 2 Instrumentation

The ASPERA-3 instrument on board of Mars Express consists of 4 sensors: the ELS sensor for thermal and energetic electrons, the IMA sensor for protons, helium and heavy ions, the time-of-flight neutral particle sensor NPD and the neutral particle sensor NPI. A general description of the instrument is given in an accompanying paper [1]. In the first part of this paper we describe how one can obtain plasma moments from the electron sensor ELS and the ion sensor IMA. For the IMA sensor we will only discuss the derivation of proton and alpha moments. Respective calculations for other ions can be made in a similar way. Specifically for heavier ions there is an additional problem of species separation. The purpose of the first part of the paper is to give a guideline and reference for the calculation of moments from the ASPERA-3 detectors. Actual calibration factors might change as the data analysis develops but we expect that the principal methods described here remain valid. Statistics of the derived moments for the environment of Mars are presented in the last section of this paper.

For the following calculations we have been using some technical documents describing calibration parameters of the ASPERA-3 sensors. These documents are not published in a journal but can be obtained from the authors. We will refer to these documents by title and main author with the remark *personal communication*.

*Instrumental Coordinates* Instrumental coordinate systems for ASPERA-3 are described in the document *ASPERA-3 sensor numbering, 3.1, (S. Barabash, pers. comm.)*. We use a coordinate system (*ASP*) which is defined as

$$X_{ASP} = Z_u = Z_{SR}, Y_{ASP} = Y_u = -X_{SR}, Z_{ASP} = -X_u = -Y_{SR} \quad (1)$$

in relation to the ASPERA-3 main unit system ( $X_u, Y_u, Z_u$ ) and the MEX spacecraft reference system ( $X_{SR}, Y_{SR}, Z_{SR}$ ). We use the same coordinate system for all ASPERA-3 sensors with azimuthal angle  $\varphi$  and polar angle  $\vartheta$  such that,  $\vartheta = 0^\circ$  is the  $Z_{ASP}$  axis and  $\varphi = 0^\circ$  is the positive  $X_{ASP}$  axis. The ASPERA-3 main unit is mounted on a rotating platform (*scanner*) but during the first two years of operation discussed in this paper the scanner was not operating. That means the ASP system as it is used here is fixed with respect to the spacecraft frame.

## 3 Plasma Moment Calculation from Particle Counters

For general introductions on moment calculations we refer the reader to textbooks, e.g. [16, 9, 17, 8]. But since textbook usually lack applied examples we list in the following the principal equations used for this paper.

We assume that each particle species can be described by a distribution function  $f(\mathbf{v})(\mathbf{v})$  in velocity space. Macroscopic properties of the particle distribution can be described by

integrals of this function folded with powers of the velocity vector:

$$\mathbf{M}^k = \int f(\mathbf{v})(\mathbf{v})^k d^3\mathbf{v}, \quad (2)$$

where  $\mathbf{M}$  is a tensor of order  $k$ .

For  $k=0$  we get the particle number density  $n$ ,  $k=1$  gives the velocity vector, normalized by  $n$ , while  $k=2$  gives us the pressure tensor. The measurable quantity for particle counters is the differential flux  $J(E, \Omega, \mathbf{r})$  for particles of energy  $E$ , at a position  $\mathbf{r}$ , within a solid angle  $d\Omega$ . If  $m$  is particle mass, the relation between the distribution function and the differential flux is:

$$J(E, \Omega, r) = \frac{v^2}{m} f(\mathbf{r}, \mathbf{v}) = \frac{2E}{m^2} f(\mathbf{r}, \mathbf{v}) \quad (3)$$

### 3.1 Moments by integration

Using equations 2 and 3 we will derive explicit forms of the moment equations. For  $k=0$  in equation 2, we get the following expression for the **density**:

$$n = \int_{\mathbf{v}} f(\mathbf{v}) d^3\mathbf{v} = \int d\varphi \int d\vartheta \sin\vartheta \int dv v^2 f(v, \vartheta, \varphi) \quad (4)$$

In the case of an isotropic plasma we get:

$$n = 4\pi \int_{\mathbf{v}} f(\mathbf{v}) v^2 dv \quad (5)$$

Using equation 3,  $v(E) = \sqrt{\frac{2E}{m}}$ , and because  $dE = mvdv$ :

$$n = \int d\varphi \int d\vartheta \sin\vartheta \int dv f(\mathbf{v}) v^2 = \int d\varphi \int d\vartheta \sin\vartheta \int dE \frac{J}{v} \quad (6)$$

If  $c(E, \varphi, \vartheta)$  are the detector counts,  $G(E, \varphi, \vartheta)$  the geometric factor of the detector,  $\tau$  the acquisition time and  $\Delta E = E_{n+1} - E_n$  the energy width of the  $n$ -th energy channel, then:

$$J = \frac{c(E, \varphi, \vartheta)}{G(E, \varphi, \vartheta) \tau \Delta E} \quad (7)$$

Note, that here we use the *solid geometric factor*  $G = \Delta A \Delta \Omega$  (sensitive surface  $\times$  solid angle) of the detector, which is usually multiplied by the detector energy resolution to define the *energy geometric factor*  $G_E = G \frac{\Delta E}{E}$ . If  $\sum_E \Delta E$  gives the full energy width of the sensor, we can substitute integrals with sums and  $dE \equiv \Delta E$ . Then:

$$n = \sum_{\varphi} \Delta\varphi \sum_{\vartheta} \Delta\vartheta \sin\vartheta \sum_E \frac{c(E, \varphi, \vartheta)}{G(E, \varphi, \vartheta) \tau v(E)}. \quad (8)$$

The general expression for the **bulk velocity**  $\mathbf{V}$  ( $k = 1$ ) is:

$$n\mathbf{V} = \int_{\mathbf{v}} \mathbf{v} f(\mathbf{v}) d^3\mathbf{v} \quad (9)$$

or explicitly:

$$\begin{aligned} nV_x &= \int d\varphi \cos\varphi \int d\vartheta \sin^2\vartheta \int dE J(E, \vartheta, \varphi) \\ nV_y &= \int d\varphi \sin\varphi \int d\vartheta \sin^2\vartheta \int dE J(E, \vartheta, \varphi) \\ nV_z &= \int d\varphi \int d\vartheta \sin\vartheta \cos\vartheta \int dE J(E, \vartheta, \varphi) \end{aligned} \quad (10)$$

For  $k=2$  we get the **thermal pressure** tensor:

$$\mathbf{P} = m \int_{\mathbf{v}} (v_i - V_k)(v_i - V_k) f(\mathbf{v}) d^3\mathbf{v} = m\mathbf{M}^2 - nmV_iV_k, \quad (11)$$

where:

$$\mathbf{M}^2 = \int_{\Omega} \int_{\mathbf{v}} v_i v_k f(\mathbf{v}) d\Omega d\mathbf{v}, \quad (12)$$

and  $i, k=(x, y, z)$  respectively, and  $V_i$  is the bulk flow.

$\mathbf{P}$  is a symmetric tensor with 9 directional elements. However, due to spatial coverage limitations of the ASPERA-3 sensor (see section 5), we will only estimate the three diagonal terms, in the ASPERA-3 coordinate system. For typical solar wind and magnetosheath plasma distributions the off-diagonal terms are negligible.

$$\begin{aligned} P_{xx} &= m \int d\varphi \cos^2\varphi \int d\vartheta \sin^3\vartheta \int dE v J(v, \vartheta, \varphi) - mV_x^2 n \\ P_{yy} &= m \int d\varphi \sin^2\varphi \int d\vartheta \sin^3\vartheta \int dE v J(v, \vartheta, \varphi) - mV_y^2 n \\ P_{zz} &= m \int d\varphi \int d\vartheta \sin\vartheta \cos^2\vartheta \int dE v J(v, \vartheta, \varphi) - mV_z^2 n \end{aligned} \quad (13)$$

and

$$P = \frac{P_{xx} + P_{yy} + P_{zz}}{3}, \quad (14)$$

$$T = \frac{P}{nK} \text{ or } T[\text{eV}] = 6241 \frac{P[\text{nPa}]}{n[\text{cm}^{-3}]}, \quad (15)$$

where  $K = \frac{1\text{eV}}{11605\text{Kelvin}}$  is the Boltzmann constant and the factor 6241 comes from conversion of units. For comparison and later use, note also:

$$1\text{nPa} = 10^{-8} \text{dyn/cm}^2 = 5.403 \cdot 10^{-12} \sqrt{\text{eV} m_e},$$

where  $m_e$  is the electron mass.

### 3.2 Moments by fitting

A different method to calculate moments of a plasma distribution is by assuming that the phase space density of particles has a Maxwellian distribution in velocity space:

$$\bar{f}(v) = C \cdot e^{-\frac{(v-\bar{v})^2}{v_t^2}}, \quad (16)$$

where  $\bar{v}$  is the bulk velocity which may be determined by integration. The constant  $C$  is determined by equation 4:

$$C = \frac{n}{(\sqrt{\pi} v_t)^3}. \quad (17)$$

Replacing the *thermal velocity*  $v_t$  by the *thermal energy* using  $v_t = \sqrt{\frac{2E_t}{m}}$  allows to express the phase space density as

$$\bar{f}(E) = n \cdot \left( \frac{m}{\pi 2E_t} \right)^{3/2} \cdot e^{-\frac{E-2\sqrt{E\bar{E}+\bar{E}}}{E_t}}, \quad (18)$$

where for the mean energy we may use:  $\bar{E} = \frac{\int_E E \cdot f(E)}{\int_E f(E)}$ .

Expressing  $E$  in [eV],  $n$  in [ $1/\text{cm}^3$ ] and  $m$  in electron masses  $m_e$ , and using  $1\text{eV} = 1.7588 \cdot 10^{15} m_e \frac{\text{cm}^2}{\text{s}^2}$  we get:

$$\bar{f}(E)[\text{s}^3/\text{km}^6] = 0.8608 \cdot 10^6 n \cdot \left( \frac{m}{E_t} \right)^{3/2} \cdot e^{-\frac{E-2\sqrt{E\bar{E}+\bar{E}}}{E_t}}. \quad (19)$$

On the other hand the phase space density for each energy channel can be expressed by the omni-directional differential flux  $J(E)$  as:

$$\bar{f}(E) = \frac{J(E)m^3}{p^2} = \frac{J(E)m^2}{2E}. \quad (20)$$

Using equation 7 we get

$$\bar{f}(E) = \frac{m^2}{2G\tau} \frac{c(E)}{\Delta E \cdot E}. \quad (21)$$

Again expressing  $E$  in [eV] and  $m$  in electron masses  $m_e$ , this is:

$$\bar{f}(E)[\text{s}^3/\text{km}^6] = \frac{0.1616m^2}{G\tau} \frac{\bar{c}(E)}{\Delta E \cdot E}. \quad (22)$$

Demanding equality between equations 19 and 22 allows to determine density  $n$  and thermal energy  $E_t$  by fitting to the measured spectrum of  $f(E)$ . When there is a positive spacecraft potential  $E_p$  the energy for each step has to be replaced by  $E - E_p$ . Since spacecraft potentials are typically less than 20eV, this correction is only important for electrons. On the other hand if plasma bulk speeds are below 300km/s, we have  $\bar{E} < 1\text{eV}$  for electrons, such that we may use  $\bar{E} = 0$  in this case.

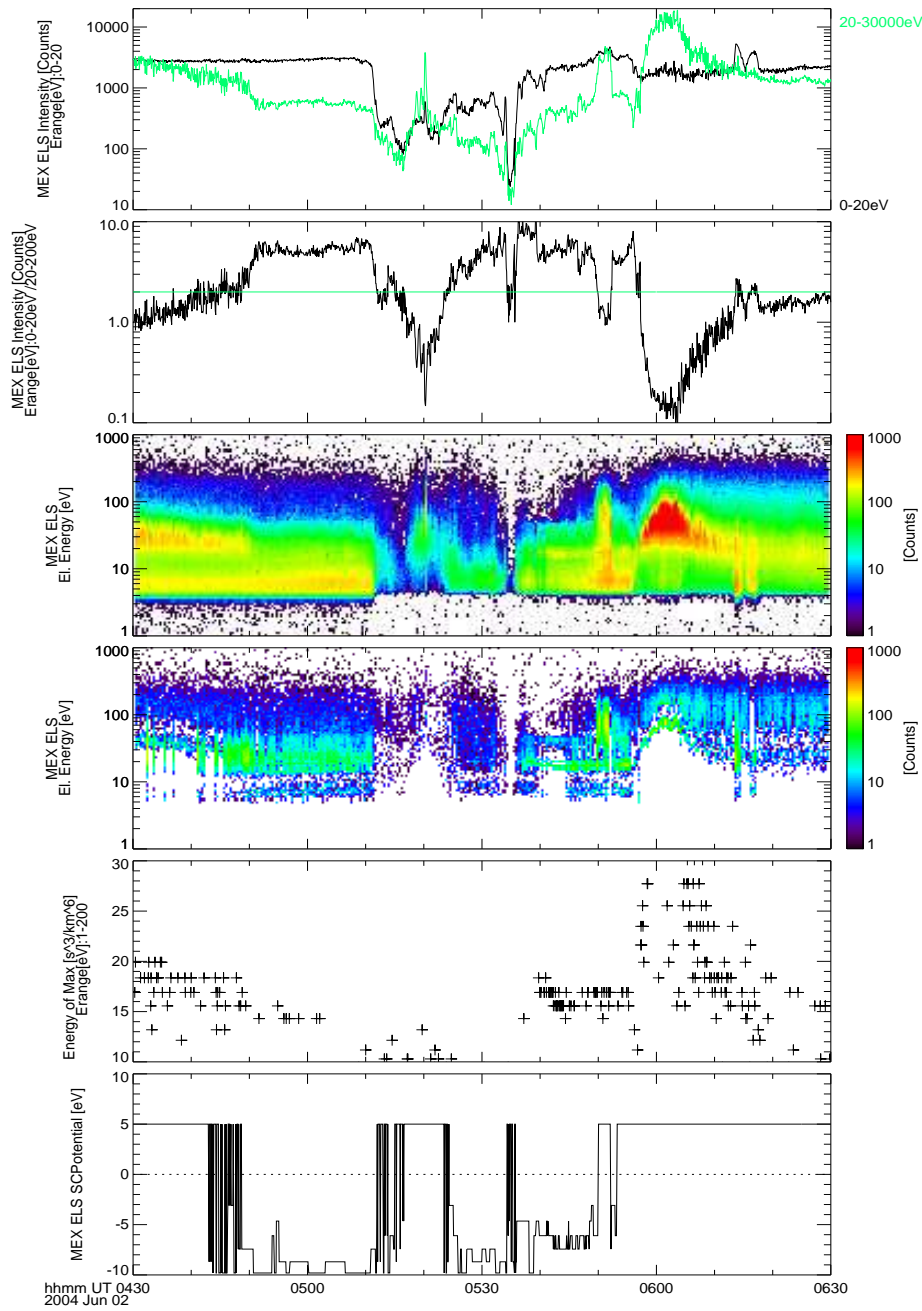


**Fig. 1** Data obtained by the ASPERA-3 ELS sensor in 2004-06-02 04:30UT to 06:30UT. Data are sampled over 4s. From top to bottom: a) counts sampled by all anodes in the energy range 0-20eV (black) and in the energy range 20-30000eV (green), b) ratio of the two quantities plotted above, c) energy spectra sampled by all anodes (counts/12s), d) same as above after subtracting an exponential fit to the phase space density for each record, e) Energy of maximum flux in the subtracted spectrum in the range 10-30eV, f) resulting spacecraft potential assuming  $\text{CO}_2$ -peak energy at 23eV.

#### 4 Electron moments from ASPERA-3 ELS

This section describes the implementation of the moment calculation for the ELS sensor of the ASPERA-3 instrument onboard Mars Express. The ELS sensor has an energy range of 0.4eV to 26keV which is split into 512 energy channels. We use the *ELS Calibration Recon\_5 of 13 Oct,2005* (R. Frahm, pers.comm.). In normal operation mode the energy steps are sampled into 128 channels. The energy allocated for each channel and the efficiency are calculated from the deflection voltages which are transmitted every 32s with the engineering data set. The geometric factor is  $G = 5.88 \cdot 10^{-4} \text{cm}^2 \text{sr}$  for each anode, but is multiplied by an efficiency factor which is linearly dependent on energy. The acquisition time for each energy channel  $\tau = 3.6/128\text{s}$ , at a sampling rate of 4s.

For the first two years of operation the ELS sensor is measuring in the plane  $\vartheta_{ASP} = 90^\circ$  and we assume spherical symmetry. This assumption may be dropped when the ASPERA-3 scanner starts operating in 2006. In this paper we assume that the scanner is not operating. Also we neglect effects of shading of the instrument by the spacecraft since the bulk flow of electrons is negligible compared to their thermal speed. We effectively only loose about a quarter of the distribution by shading resulting in a relatively small underestimation of the density. This is different for higher energetic electron beams in the ionosphere which we do not discuss in this paper.

The quantity defined via the calibration procedure for each anode and energy step is the differential flux

$$J(E, \varphi) [\text{c}/(\text{cm}^2 \text{ s sr eV})] = \frac{c(E, \varphi) S_{adj}(\varphi)}{G_{eff}(E, \varphi) \tau} \quad (23)$$

where  $c(E, \varphi)$  are the raw counts for each bin,  $S_{adj}(\varphi)$  is a time constant *science adjustment* for each anode and  $G_{eff} [\text{cm}^2 \text{ sr eV}]$  contains energy resolution and efficiency of each anode and is further described in the calibration document.

Using this we get from equation 8 the final expression for the **density**:

$$n [\text{cm}^{-3}] = \frac{\pi}{4} \cdot 1.686 \cdot 10^{-8} \sqrt{m[m_e]} \sum_{\varphi} \sum_E \frac{J(E, \varphi) \Delta E}{\sqrt{E[\text{eV}]}} \quad (24)$$

The factor appears as a result of the conversion of Joule to eV (see equation 19) and  $\Delta\varphi \int_0^\pi d\vartheta \sin\vartheta = \frac{\pi}{4}$ , if we assume that the value observed at each anode is valid for all values of  $\vartheta$ . Alternatively one can regard this factor as the anode average multiplied by  $4\pi$ .  $\Delta E$  is the energy width of each channel obtained by taking the difference between the center energies.

The calculation of the three **velocity** components is done with respect to the ASP coordinate system (see section 2). Since ELS is scanning on a plane, it is not possible to estimate the velocity in the z- direction (this will change if the ASPERA-3 scanner operates.) Therefore the measurement is only dependent on the angle  $\varphi$ , between the x- direction as defined in the ASP coordinate system and the viewing direction of each of the 16 ELS anodes. For  $\vartheta=90^\circ$  by using equations 3, 7, and 10 we get:

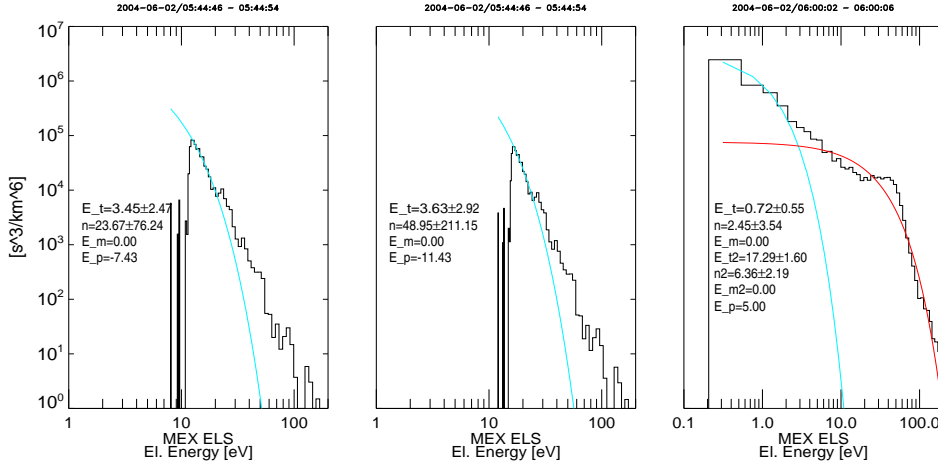


**Fig. 2** Phase space density as a function of energy, obtained by the ASPERA-3 ELS sensor in the ionosphere at 2004-06-02 05:44:46UT to 05:44:58UT. Data are sampled over 4s. The black lines are the measured data, the blue lines are exponential fits assuming the spacecraft potential value  $E_p$  ( $\text{CO}_2$  peak at 23eV) and mean energy  $E_m = 0\text{eV}$ . The red lines are fits to the high energy part of the distribution. Fit parameters  $n$  [ $1/\text{cm}^3$ ] and  $E_t$  [eV] are given for each fit with respective standard deviations.

$$nV_x[\text{km/s}] = \frac{\pi^2 10^{-5}}{16} \sum_{\varphi} \cos(\varphi) \sum_E J(E, \varphi) \Delta E \quad (25)$$

$$nV_y[\text{km/s}] = \frac{\pi^2 10^{-5}}{16} \sum_{\varphi} \sin(\varphi) \sum_E J(E, \varphi) \Delta E$$

$$nV_z \equiv 0$$

where  $c(E, \varphi)$  are the counts recorded by each ELS anode at an angle  $\varphi$  with respect to the x- direction. The factor  $\pi^2/16$  defines the solid angle of integration:  $\Delta\varphi \int d\vartheta \sin^2 \vartheta$ .

For the thermal **pressure**, as in the case of the velocity calculation, we can analyze only the dependency on the  $\varphi$  angle and therefore we set  $P_{zz} \equiv 0$ . In total:

$$P_{xx}[\text{nPa}] = \frac{5.403 \cdot 10^{-12} \pi}{12} \sum_{\varphi} \cos^2 \varphi \sum_E \sqrt{E} J(E, \varphi) \Delta E - mV_x^2 n \quad (26)$$

$$P_{yy}[\text{nPa}] = \frac{5.403 \cdot 10^{-12} \pi}{12} \sum_{\varphi} \sin^2 \varphi \sum_E \sqrt{E} J(E, \varphi) \Delta E - mV_y^2 n$$

$$P_{zz} = 0$$

where  $\pi/12 = \Delta\varphi \int d\vartheta \sin^3 \vartheta$  and a factor from conversion of units (see equation 15). The velocity and pressure formulas are provided only for completeness. Since measurement of the bulk flow with a planar sensor, which is partly shadowed by the spacecraft, produces large errors it is better to calculate the thermal pressure from the thermal temperature obtained by fitting the energy spectrum.

#### 4.0.1 Spacecraft Potential

Fig.1 shows data obtained by the ELS-sensor for the period 2004-06-02 05:30UT to 06:30UT. The third panel from top shows the energy spectrum in raw counts obtained by the sensor. We generally work with spectra obtained by integrating all 16 anodes. The drop in counts below 5eV is caused by a -5V repeller voltage applied to protect the anode counters from saturation. In consequence the low energy part of the spectrum is hidden from observation.

Between 04:30 and 04:50 the sensor observes high count rates above 20eV. Here the spacecraft crosses the magnetosheath. Between 04:50 and 05:55 the spacecraft crosses the magnetosphere with a wake crossing from 05:10 to 05:40. After 05:55 the spacecraft crosses the sheath again and enters the solar wind at 06:15. Experience with other missions shows that in the ionosphere the spacecraft is usually negatively charged and positively outside. To estimate the spacecraft potential for a specific time we first have to determine whether the distribution is ionospheric or not. For this discrimination we use the ratio of counts obtained above and below 20eV (panel 2 from top). If this ratio exceeds the value 3 we call the distribution ionospheric otherwise non-ionospheric. We observe that e.g. in the wake this criterion declares distributions non-ionospheric. For non-ionospheric distributions we assume a constant potential of either 0V or +5V. Unfortunately with this criterion sometimes spectra obtained in the solar wind are also classified ionospheric when SC photo electrons are present. To avoid this we apply an additional criterion demanding that a photo-electron peak determination must be possible within a 20 min time interval around the timetag of the data sample.

As can be seen from Fig.2 for ionospheric spectra a local peak in the spectrum can sometimes be observed between 10 and 25eV (here especially between 05:40 and 05:55). This peak corresponds to O<sub>2</sub> and CO<sub>2</sub> photo electrons and is expected to have an actual energy between 21 and 28eV [13]. Actually there are two peaks expected (and sometimes observed) at 23 and 27eV energy. The identification of these photo-electrons is discussed in detail by [6]. We determine the observed energy of this peak by subtracting the low energy thermal part of the spectrum using an exponential fit to the phase space density (panel 4 from top of Fig.1). The energy of the maximum phase space density in the range 10 to 30eV is shown in the bottom panel. We now subtract either 23eV or 27eV from this energy to estimate the SC potential for ionospheric distributions. If for a specific point in time a CO<sub>2</sub>-peak cannot be determined we take the value from the spectrum closest in time for which a value can be determined. To correct the distribution for the spacecraft potential we subtract the potential from the instrumental energy for each channel. Note, that this method does not exclude SC photo electrons or secondary electrons. The geometric factor and energy resolution of the sensor are a function of the actually measured energy, thus they are not affected by the shift in energy applied to the data after applying the geometric factors.

#### 4.1 Discussion of ELS spectra and moments

Fig.2 shows phase space densities as a function of energy calculated from the same data as in Fig.1 for some 4s-spectra obtained in the ionosphere (a,b) and magnetosheath (c). In Fig.2a we assume the CO<sub>2</sub>-peak to be at 23eV to determine the SC potential ( $E_p$ ). We further assume that the mean electron energy ( $E_m$ ) is 0eV. Then we fit an exponential to the 10 energy bins with energies larger than the bin with maximum flux. The resulting fit is shown in blue and the fitted values for temperature  $E_t$  and density  $n$  are given with their standard deviations. We observe that the standard deviation for the temperature is usually lower than  $E_t$ , while the

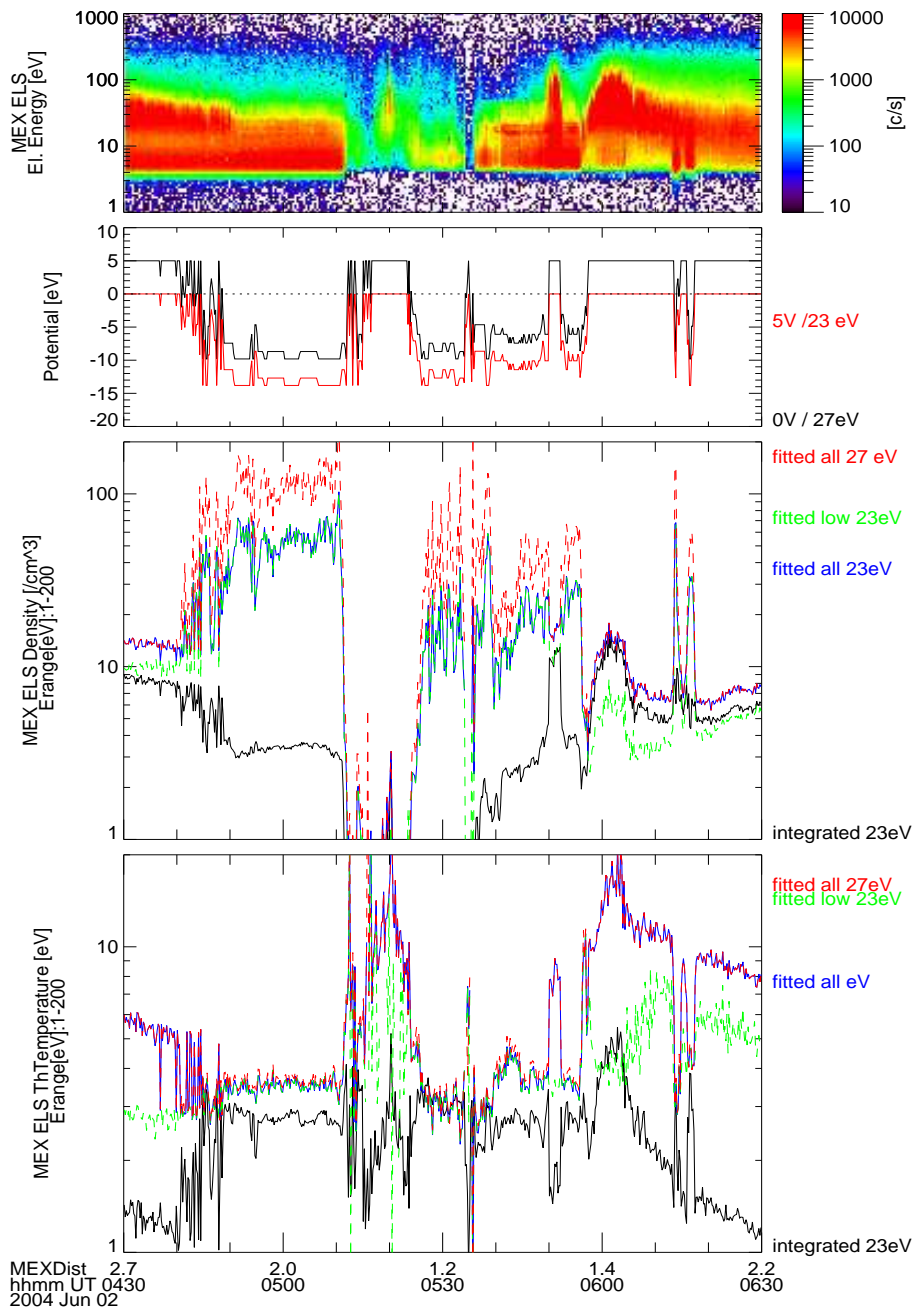


**Fig. 3** Data obtained by the ASPERA-3 ELS sensor in 2004-06-02 05:30UT to 06:30UT. Data are sampled over 4s. From top to bottom: a) energy colour spectrum of the integrated counts/12s of all anodes, b) space craft potential assuming +5V outside the ionosphere and  $\text{CO}_2$  peak energy at 23eV, b) densities [ $\text{cm}^{-3}$ ] derived from calibrated data assuming the SC potential above by integration (black), by fitting over the low energy part of the spectrum (green) and the complete spectrum (blue), c) total temperatures [eV] by the same methods.

density has very large standard deviations. This reflects the uncertainty in the extrapolation to 0eV energy which essentially determines  $n$ .

Fig.2b shows the same distribution assuming that the CO<sub>2</sub>-peak is at 27eV. We observe that the density is rather sensitive to the assumed space craft potential.

Fig.2c shows a distribution measured in the magnetosheath assuming a SC potential of +5V. Here the high energy part of the distribution (from 10 channels above the energy of maximum flux) is fitted as well (red line) resulting in the partial density  $n_2$  and temperature  $E_{t2}$ . Note, that the bump at 50-80 eV is better fitted assuming a high mean energy  $E_{m2}$  for the high energy part. But since this would correspond to a very high differential streaming velocity of the high energy part we assume  $E_{m2} = 0$ .

Fig.3 shows again data obtained by the ELS-sensor for the same time interval as Fig.1. The top panel shows an uncalibrated energy spectrum in counts/s taken from 12s averages of the original data. The second panel shows the SC potential estimate, which here is set to +5V for non-ionospheric distributions and calculated from a 23eV CO<sub>2</sub> peak for ionospheric distributions (black line). When setting the potential to 0V for non-ionospheric distributions and calculate it from a 27eV CO<sub>2</sub> peak for ionospheric distributions we obtain the potential shown by the red line. The third panel shows electron density estimates by integration (black), by fitting the low energy peak (green) by fitting low and high energy parts with the first SCPotential estimate (blue) and with the second SCPotential estimate (red). One can see that for ionospheric distributions the integrated density is far off from the expected value, while outside the ionosphere they are off by a factor 2. Note also, that for ionospheric distributions there is no fit to the high energy part of the spectrum.

The bottom panel shows temperature estimates by the same methods. Here we observe that for ionospheric distributions fitted and integrated temperatures are comparable, while in the sheath and solar wind the high energy part determines the total temperature. Total temperature has been calculated by

$$T_{total} = \frac{T_{low}n_{low} + T_{high}n_{high}}{n_{low} + n_{high}}. \quad (27)$$

We observe that for the alternative SCPotential estimate for non-ionospheric densities values do not change significantly, while for ionospheric densities values increase by a factor 2. Temperatures are unaffected for both cases.

For magnetosheath and solar wind the observed values of 1-10 e/cm<sup>3</sup> appear to be reasonable, but in the ionosphere at altitudes of about 300km we might expect densities well above 1000 e/cm<sup>3</sup> - as reported by plasma frequency measurements (E.Nielsen, MARSIS - personal comm.). Though there is a lot of uncertainty in this value at higher altitudes. The reason for this discrepancy is probably that at lower altitudes the electrons have a core temperature of less than 1eV such that the energy resolution of the ELS sensor is insufficient when the spectrum is shifted by a negative SC-potential.

Electron velocity and temperature determinations are discussed at the end of this paper in context with IMA observations. On about one orbit per month the sensor is operated in *linear stepping mode*. In this mode the energy range of the sensor is restricted to 0-128eV divided into linear steps of 1eV. In this mode the -5V repeller voltage mentioned above is switched off. Analysis of sample spectra shows that the problems related to the extrapolation of the spectrum at negative space craft potential is present as well and the quality of derived moments does not increase substantially in this mode.

## 5 Ion moments from ASPERA-3 IMA

The IMA sensor of the ASPERA-3 instrument is a combined electrostatic energy- and magnetic mass-analyzer. It measures mass/charge and energy/charge of ions in the ranges 1-30amu/e and 10-30000eV/e. The instrument uses 16 anodes covering the ASP-XY plane. The ASP polar angle is measured by electrostatic deviation covering  $45^\circ \leq \vartheta_{ASP} \leq 135^\circ$  in 16 sectors during a sampling time of 192s. For each anode and sector mass/charge is measured in 32 channels (*massrings*) by magnetic deviation and energy/charge in 96 energy channels.

The instrument operates at 3 different post-acceleration voltages (PAC) to allow increased energy and mass resolution depending on the plasma environment. These PAC levels are: PAC0: 90V, PAC1:2433V, PAC2:4216V. The efficiencies and energy range depend on the PAC level. The PAC level for a specific data record can in principle be taken from the PAC high voltage monitor variable in the IMA house keeping (HK) dataset. In practice there is a timetag mismatch between HK timetags and data record timetags. We apply an algorithm which searches for the last valid HK record for each data record.

The ground calibration of the instrument is described in *MEX IMA Calibration. Final Report. V3.0,2005 (A. Fedorov,pers.comm, cited hereafter as IMACalRep)*. This report essentially covers the determination of geometric factors as a function of energy for different ion species by lab measurements. Inflight calibrations are covered by the documents *Mars Express ASPERA-3.Flight Tables, 2006 (A. Fedorov,pers.comm)* and *IMA ASPERA-3 MEX. What happened with the low energy ions?,2006 (A. Fedorov,pers.comm)*. The essential result of these calibrations is that the effective number of energy channels is reduced to 54 – caused by an unexpected voltage on one of the deflector plates.

In the following sections we discuss observations made when analysing the actual inflight data. We try to determine noise reduction algorithms and efficiencies of the different mass-rings and anodes before we proceed to the moment calculations. There are many different ways to reduce noise in measured data. We here describe the methods which we regard as best suited for the IMA dataset.

**Geometric factors**  $GF_L$  for  $He^{++}$ ,  $O^+$  and  $O_2^+$  for the 3 PAC levels have been calculated in the IMACalRep from lab measurements. These factors contain the energy resolution  $\Delta E/E$  and are integrated over the polar angle  $\vartheta$ . That means the angular width  $\Delta\vartheta$  must not be applied in the integrations and we define  $G = GF_L E/\Delta E$  in the following equations. We use tables 5-7 of the IMACalRep and apply the  $He^{++}$  factors to  $H^+$  and  $He^+$ , the  $O^+$  factors to  $O^+$  and  $O^{++}$  and the  $O_2^+$  factors to heavier ions. As mentioned above we do not apply the massring dependency of  $GF_L$  discussed in section 7 of the IMACalRep. We also do not take account of the  $\varphi$  and  $\vartheta$  dependencies of  $GF_L$  within each anode and sector range. The principal dependence on  $\varphi$  and  $\vartheta$  is covered by the corrections discussed above. Towards the borders of each anode the efficiency decreases by about 50%. A correction for this effect would alter the calculated density by less than 2. We expect that application of the minor efficiency corrections do not have a significant influence on the derived moments. Another problem is the sampling of a cold ion beam - as the solar wind, which usually has an angular spread of less than 5deg. Since the IMA sensor has angular bins of  $22.5deg \times 5.8deg$  the beam should usually be observed in only one bin and the geometric factor will be overestimated. In fact there seems to occur some scattering in the sensor which causes signals in the neighboring spatial bins as well. For this reason when calculating core densities we sum the counts of all spatial bins but take the geometric factor for one bin only as we do in this paper. But when calculating the spectrum for non-beam distributions (e.g. pick-up ions) it is better to take the

maximum spatial bin value for each energy level. This is discussed in the context of pick-up ions in another paper [5].

The integrated **density** can either be determined by integrating over a complete 192s scan or by just using one  $\varphi$ -scan for a fixed  $\vartheta$ . For a complete scan we get:

$$n[\text{cm}^{-3}] = \frac{\pi \cdot 7.1987 \cdot 10^{-7} \sqrt{m[\text{amu}]}}{8G[\text{cm}^2\text{rad}]\tau[\text{s}]} \sum_{\varphi} \sum_{\vartheta} \sin \vartheta \sum_E \frac{c(E, \varphi, \vartheta)}{\sqrt{E[\text{eV}]}} \quad (28)$$

where we use  $\Delta\varphi = 2\pi/16$  and unit conversion as in equation 19.

For the **velocity** we have to use the complete scan:

$$\begin{aligned} nv_x[\text{km/s}] &= \frac{\pi 10^{-5}}{8G[\text{cm}^2\text{rad}]\tau[\text{s}]} \sum_{\varphi} \cos \varphi \sum_{\vartheta} \sin^2 \vartheta \sum_E c(E, \vartheta, \varphi) \quad (29) \\ nv_y[\text{km/s}] &= \frac{\pi 10^{-5}}{8G[\text{cm}^2\text{rad}]\tau[\text{s}]} \sum_{\varphi} \sin \varphi \sum_{\vartheta} \sin^2 \vartheta \sum_E c(E, \vartheta, \varphi) \\ nv_z[\text{km/s}] &= \frac{\pi 10^{-5}}{8G[\text{cm}^2\text{rad}]\tau[\text{s}]} \sum_{\varphi} \sum_{\vartheta} \sin \vartheta \cos \vartheta \sum_E c(E, \vartheta, \varphi) \end{aligned}$$

But velocity and pressure can only be determined when the bulk flow is in the instruments  $\vartheta$ -range. Fortunately this is the case for most orbits when the spacecraft is in the solar wind and magnetosheath. For regions with low bulk flow speed as for example heavy ions in the ionosphere one has to apply a correction for the partial field of view of IMA.

For the integrated kinetic **pressure** we might again assume spherical symmetry, such that we get from equation 13 and 15:

$$P_{xx}[\text{nPa}] = \sqrt{m[\text{m}_e]} \frac{5.403 \cdot 10^{-12} \pi}{8G[\text{cm}^2\text{rad}]\tau[\text{s}]} \sum_{\varphi} \cos^2 \varphi \sum_{\vartheta} \sin^3 \vartheta \sum_E \sqrt{E[\text{eV}]} c(E, \vartheta, \varphi) \quad (30)$$

$$P_{yy}[\text{nPa}] = \sqrt{m[\text{m}_e]} \frac{5.403 \cdot 10^{-12} \pi}{8G[\text{cm}^2\text{rad}]\tau[\text{s}]} \sum_{\varphi} \sin^2 \varphi \sum_{\vartheta} \sin^3 \vartheta \sum_E \sqrt{E[\text{eV}]} c(E, \vartheta, \varphi) \quad (31)$$

$$P_{zz}[\text{nPa}] = \sqrt{m[\text{m}_e]} \frac{5.403 \cdot 10^{-12} \pi}{8G[\text{cm}^2\text{rad}]\tau[\text{s}]} \sum_{\varphi} \sum_{\vartheta} \sin \vartheta \cos^2 \vartheta \sum_E \sqrt{E[\text{eV}]} c(E, \vartheta, \varphi) \quad (32)$$

The thermal pressure is calculated from this by

$$\mathbf{P}_{th}[\text{nPa}] = \mathbf{P}_{kin} - m[\text{m}_e] 9.1 \cdot 10^{-10} \mathbf{V}^2 n \quad (33)$$

and total temperature by

$$T_{th}[\text{eV}] = 6241 \frac{\text{Trace}(\mathbf{P}_{th})}{3n}. \quad (34)$$

As for the ELS sensor the better estimate of the total pressure can be obtained by using a fit to the energy spectrum since the integrated pressure is rather sensitive to noise in the data.

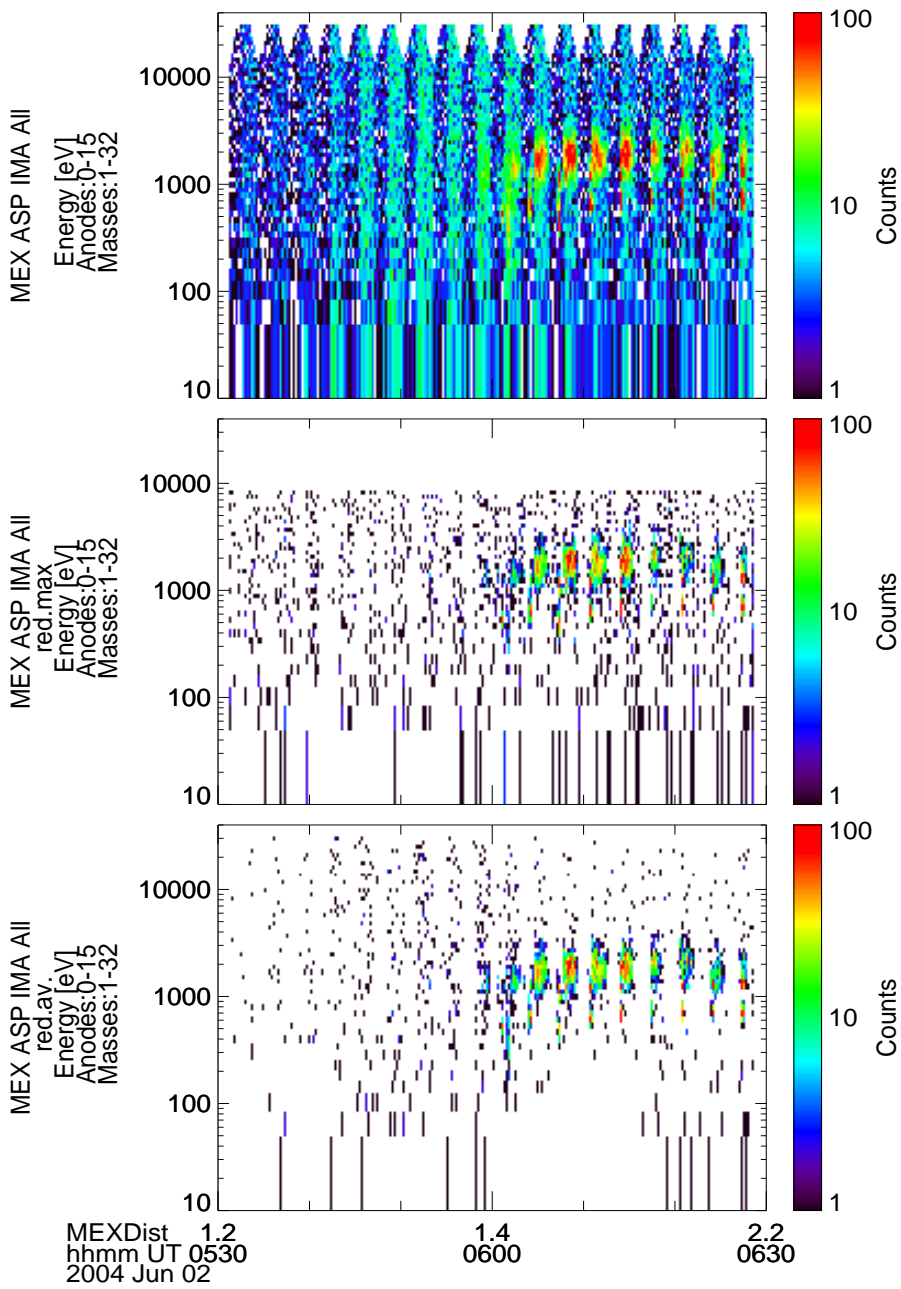


**Fig. 4** Noise reduction in absolute counts obtained by the ASPERA-3 IMA sensor in 2004-06-02 05:30UT to 06:30UT as a function of energy/charge. Shown are sums over all 16 anodes and 32 massrings. Data are sampled over 12s. Panels show from top to bottom: a) Unreduced counts, b) counts after subtracting the maximum count observed in the 15 top and bottom energy channels, c) counts after subtracting the average counts for each 192s dataset from each bin of the  $96 \times 32 \times 16$  matrix..

## 5.1 Noise Reduction

Observation of the measured spectra shows that the IMA sensor is sensitive to different sources of noise: electronic noise of the amplifiers, noise caused by penetrating electrons and high energy protons depending on solar activity, noise caused by UV light depending on spacecraft orientation.

Fig.4 shows energy spectra obtained by IMA for the same period of time as discussed in the previous section for the ELS sensor. The top panel shows the unreduced counts integrated over all 16 anodes and 32 massrings for each  $\vartheta$ -sector sampled over 12s. The polar scan covering 192s shows up in the repeatable pattern of the data. In the ionosphere before 05:40 data seem to contain just noise, between 05:40 and 06:10 the noise level increases - presumably caused by UV-light, after 05:55 solar wind ions appear at 1-4 keV energy.

We observe that the noise affects all energy channels and massrings in comparable levels. We apply two different techniques to reduce the noise level: 1. (*reduce by maximum method*) Since valid ion data are usually observed in the energy range 50eV-8keV we determine for each anode and sector the maximum count rate above 8keV and below 40eV (top and bottom 15 energy channels) and subtract this rate from all bins. 2. (*reduce by average method*) We subtract from all bins of the  $96 \times 32 \times 16 \times 16$  matrix the mean counts of all non-zero bins.

Results of the two noise reduction methods are shown in the lower panels of Fig.4. We observed qualitatively that the first method is sufficient for most data records in reducing the noise level such that the reduced background is negligible compared to the valid signal. Only for records with severe UV contamination the second method is more recommendable. We also tested a *third method* which neglects all bins of the  $96 \times 32 \times 16 \times 16$  matrix which contain just a single count, but we observed that this method severely affects the valid signal. Nevertheless this method has been applied onboard to IMA data after Oct 11, 2005 because high solar activity in summer 2005 increased the IMA background noise level in such a way that the allowed data transmission rate was exceeded.

## 5.2 Mass Ring Efficiencies

Fig.5a shows an IMA energy/mass matrix without noise reduction for 2004-06-02 06:17-06:19UT (PAC1). Overplotted are expected ion species ranges for PAC1 (see section 5.4). The track marked by black lines is for protons, the one by green lines for  $\text{He}^{++}$ -ions. We observe: 1. The efficiency of different massrings is different, specifically massrings 1,5 and 17 have higher count rates than the neighboring rings. 2. There is a trace of higher count rates between 800 and 1500eV which is presumably caused by protons for which the massring allocation did not work. We call these *spill-over protons* since their signal is appearing in mass rings where no protons are expected.

To take account of both effects we calculated integrated count rates for each massring accumulated between 2004-02-01 and 2005-10-10 (Fig.6). We observe that massring 1 contains most counts by far. The other massrings behave similarly for the different PAC levels. Massrings 11 and 23 are virtually empty, massrings 5 and 17 are unusually high, above massring 15 even massrings have lower efficiency. Inspection of individual matrices also revealed that the high counts in massring 1 coincide with spill-over protons. We now assume that the massring 1 counts for each energy level can be taken as a measure of spill-over protons in that energy channel. To obtain the relative massring contamination by spill-over protons we integrated the massring totals only for those periods where massring 32 contains more

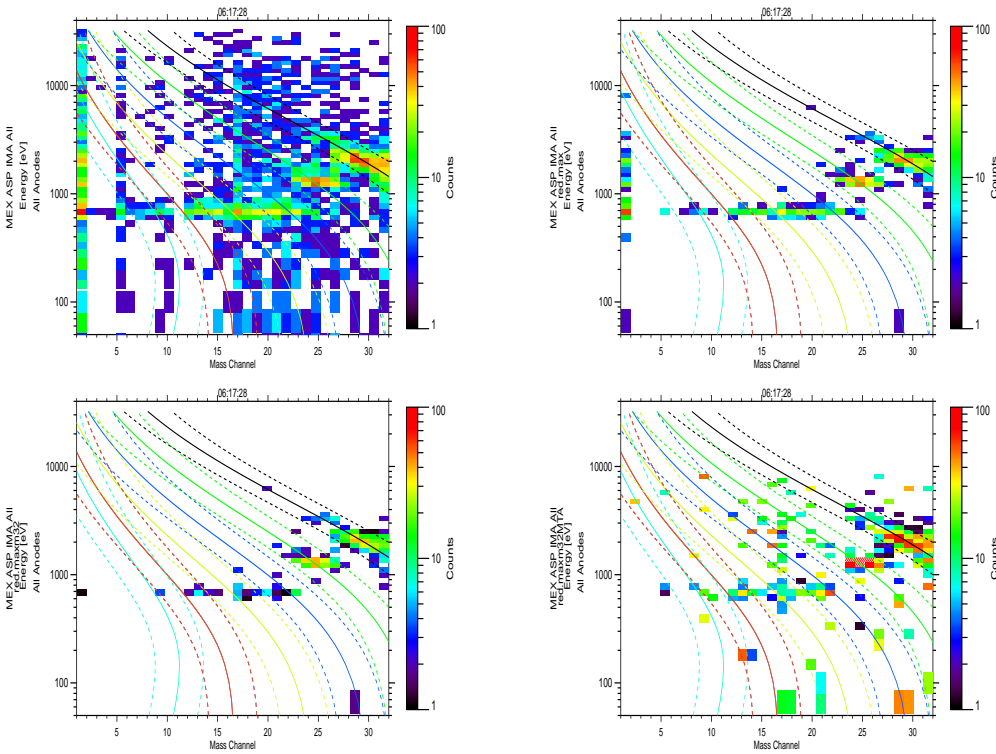


**Fig. 5** ASPERA-3 IMA energy/mass matrix obtained on 2004-06-02 06:17-06:19UT. Overplotted are expected ion species ranges for PAC1. Absolute count rates: a) without reduction, b) after maximum reduction, c) after proton subtraction, d) after application of efficiencies.

than 2000 counts. We assume that these periods are representative for high proton contamination. To subtract spill-over protons from a data record we subtract from each bin in the  $96 \times 32 \times 16 \times 16$  matrix the massring 1 counts multiplied by the massring efficiency. The result is shown in Fig.5c. We observe that the reduction is not perfect but by far the best method we have obtained so far.

To determine the relative efficiencies of neighboring massrings we apply a 3rd order polynomial fit to the massring totals summed over energy and spatial bins - relative to the counts observed in massring 1 observed for periods with massring 32 counts of less than 2000. This gives us a measure of the background noise in the different massrings. The result is shown in Fig.6. Each massring gets an efficiency correction defined by the ratio between the measured counts and the fit.

### 5.3 Anode and Theta Efficiencies

Fig.7 shows the total counts (integrated over energy and mass) relative to the maximum total counts observed for each 192s-record for the 16 anodes and 16  $\vartheta$ -sectors of the IMA sensor. We observe that anodes 1-3 have a count level about 4 times higher than the other anodes. One reason for this is that the sensor orientation is on most orbits such that these anodes

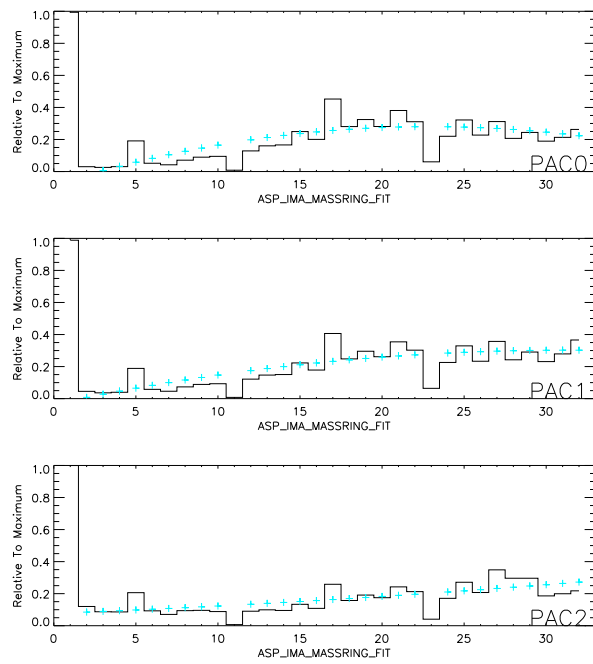


**Fig. 6** ASPERA-3 IMA total counts for the 32 different massrings for the 3 PAC levels for data obtained between 2004-02-01 and 2005-10-10. The blue crosses show a 3rd order polynomial fit to the data - excluding bins without cross.

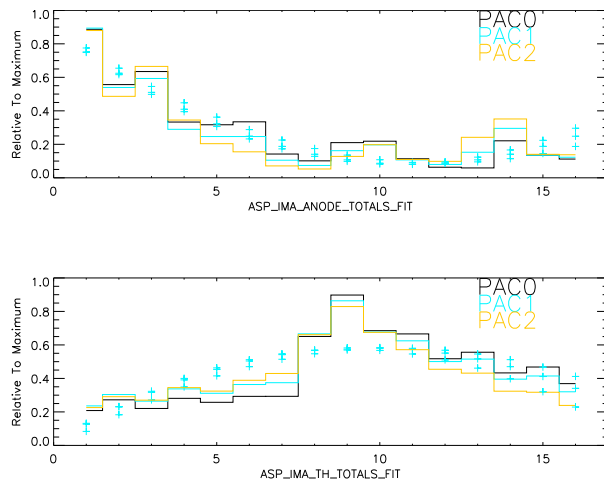


**Fig. 7** ASPERA-3 IMA total counts (relative to maximum) for the 16 different anodes (top) and the 16 different sectors (bottom) for the 3 PAC levels (colored) for data obtained between 2004-02-01 and 2005-10-10.

obtain the bulk solar wind flux. On the other hand we would then expect a comparable flux level in the neighboring anode 16. Lab measurements did not show significant differences in anode efficiency (A.Fedorov, pers.comm.). We assume that the large differences in anode count rates are partially caused by shading of the sensor by the spacecraft and generally apply the correction factors corresponding to Fig.7a.

The later is also true for the sector efficiency (Fig.7b). Sectors 1-8 are looking towards the spacecraft and show much lower count rates. In principle plasma moments can only be determined when the bulk flow of plasma is in sectors 9-14. In Fig.5d massring, anode and sector efficiencies have been applied.

#### 5.4 Species Separation

For each PAC level the IMA sensor has a different measurement range for the ion species in massring and energy. These ranges are taken from a formula in *Mars Express ASPERA-3.Flight Tables, 2006* (A. Fedorov,pers.comm). The formula delivers an upper and lower massring number for a given mass/charge for each energy and PAC level.

Fig.8a shows an uncalibrated spectrum for orbit 539, which was discussed in [4]. We take this orbit as an example to discuss species separation because it contains solar wind light ion and ionospheric heavy ion observations.

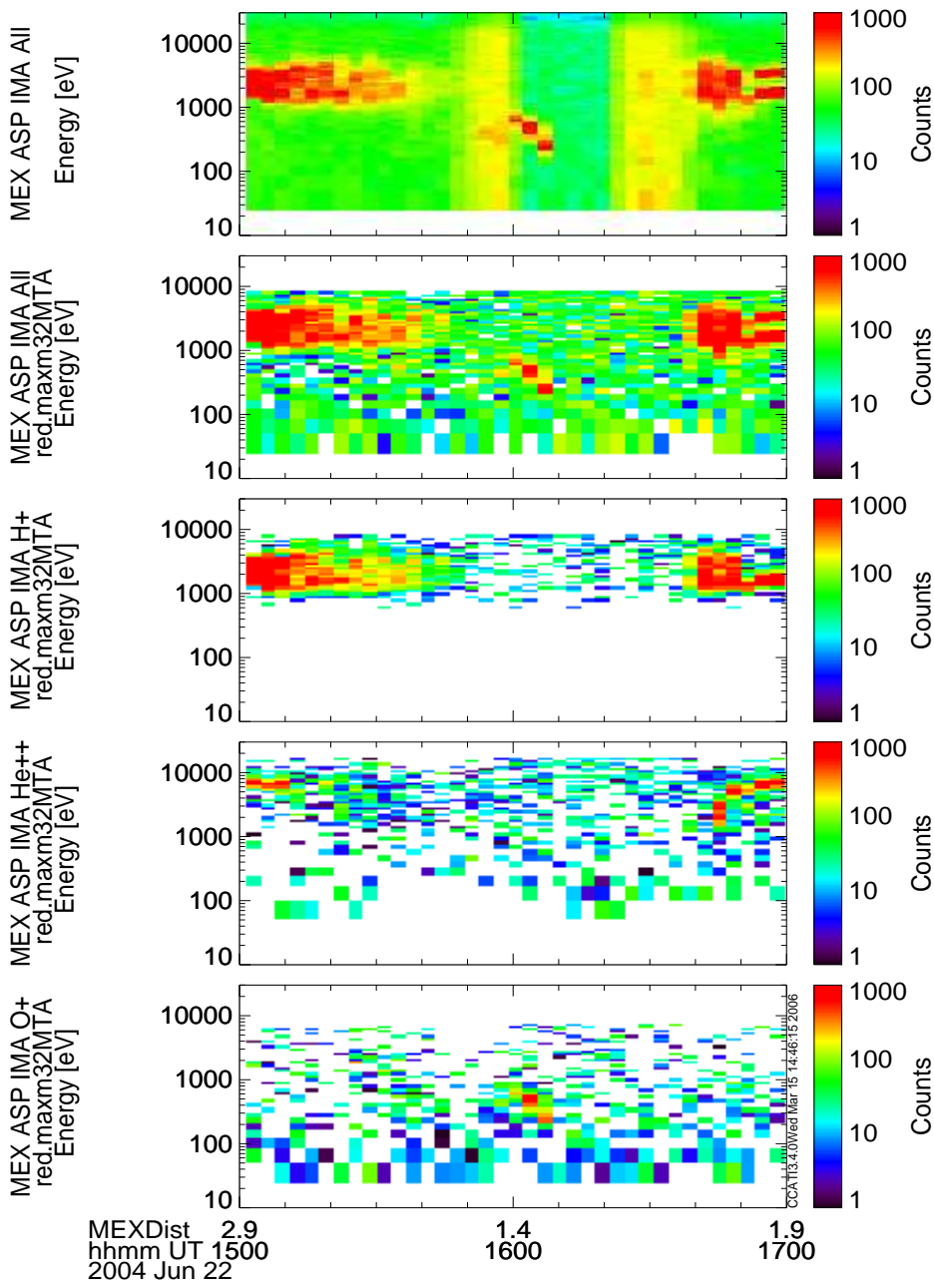
Fig.9(top left) shows an IMA energy/mass matrix obtained at 15:02 on this orbit. Overplotted are expected ion species ranges for PAC1 for mass/charge ratios 1( $H^+$ ), 2( $He^{++}$ ), 4( $He^+$ ), 8( $O^{++}$ ), 16( $O^+$ ) and 32(> $O^+$ ). From the species ranges we calculate a probability matrix for each species where for each energy channel  $E$  and massring  $m$  the probability to contain species  $s$  is:

$$P_s(E, m) = e^{\left(\frac{m-c_s(E)}{b_s(E)}\right)^6}, \quad (35)$$

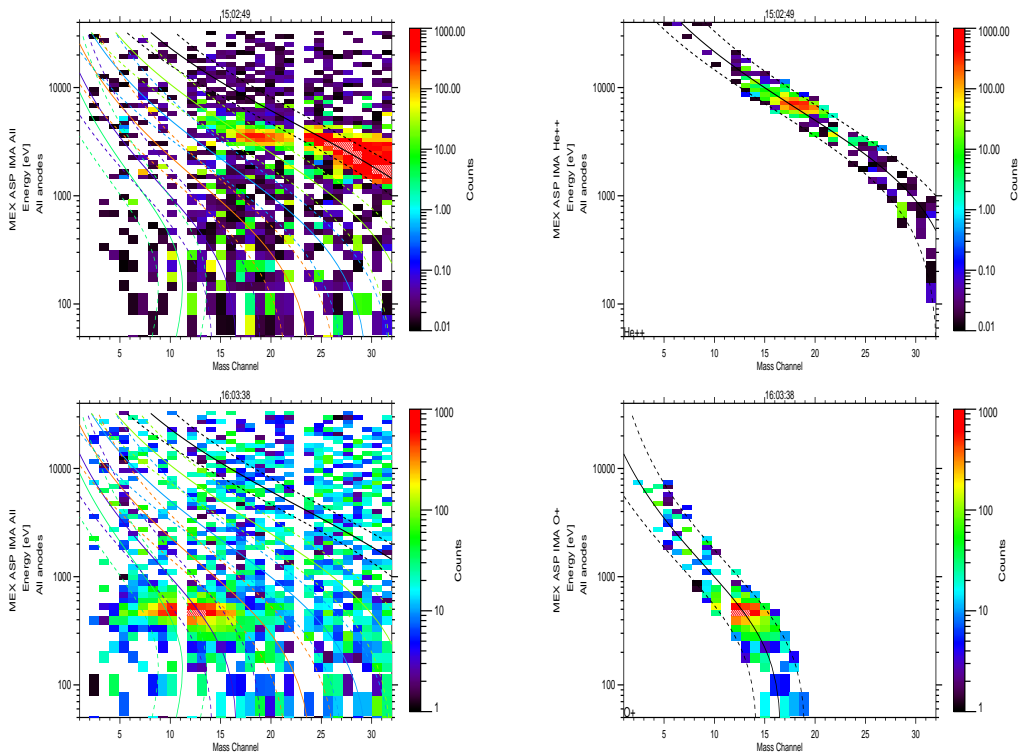
where  $c_s(E)$  is the center massring number and  $b_s(E)$  the massring range for each species and energy step. While the probability distribution underlying the tracks is Gaussian [4, IMACalRep], we empirically determined the exponent 6 to avoid the loss of counts within the species range. On the other hand we loose valid counts outside of the range. In principle one has to apply an efficiency correction taking account of a decrease in efficiency with distance from the track center as described in section 7 of IMACalRep, but since this is a second order effect we here do not apply this correction.

Fig.9(top right) shows the matrix after multiplication with  $P_{He^{++}}(E, m)$  and multiplying energies by a factor 2 to account for the ion charge. Fig.9(bottom left) shows the matrix obtained at 16:03 containing heavy ions. This matrix is also shown in Fig.3 of [4]. Note, that in [4] massring 11 - which is virtually empty - is replaced by an average of the neighboring massring counts to achieve a smooth dataset for species fitting. Note, also that for the heavy ion matrix we did not apply a noise reduction to get a comparable result to [4].

Fig.9(bottom right) shows the matrix after multiplication with  $P_{O^+}(E, m)$ . The lower panels of Fig.8 show the energy spectra as a function of time after applying  $P_s(E, m)$  for different ion species.



**Fig. 8** ASPERA-3 IMA energy spectra obtained between 2004-06-22 15:00 and 17:00UT. From top to bottom: a) non-reduced, uncalibrated counts integrated over anodes, massrings and sectors, b) after noise reduction and calibration, c) after selection of  $H^+$  trace, d) after selection of  $He^{++}$  trace, e) after selection of  $O^+$  trace.



**Fig. 9** ASPERA-3 IMA energy/mass matrix obtained on 2004-06-22 15:02(top) and 16:03(bottom). Top panels are noise reduced. All panels are calibrated. The left panels contain all counts. Right panels just  $\text{He}^{++}$  (top) and  $\text{O}^+$  (bottom) tracks. Overplotted are expected ion species ranges for PAC1.

## 5.5 Resulting IMA moments

### 5.5.1 Proton Density

Fig.10 shows data obtained by ASPERA-3 ELS and IMA obtained between 2004-08-01 03:00 and 04:00UT. The top panel shows the energy spectrum obtained by the ELS sensor. The interval contains a period in undisturbed solar wind (until 03:15), magnetosheath (until 03:40), ionosphere (until 03:55) and wake (from 03:55). We calculate high energy electron densities (second panel) of  $2\text{-}3/\text{cm}^3$  in the solar wind, and of  $4\text{-}10/\text{cm}^3$  in magnetosheath. In the ionosphere fitted electron densities are calculated at  $20\text{-}40/\text{cm}^3$ .

The third panel from top of Fig.10 shows the sectorized uncalibrated IMA energy spectrum. The fourth panel shows proton densities calculated by integration without application of noise reduction and calibration factors (but application of geometric factors). If we calculate densities for each sector separately (black line) we assume symmetry of the distribution when rotating around the sector ring. This only makes sense when the peak flux is contained in the respective sector ring. The  $4\pi$ -integrated density (green line) is essentially the integral over the sectorized densities.

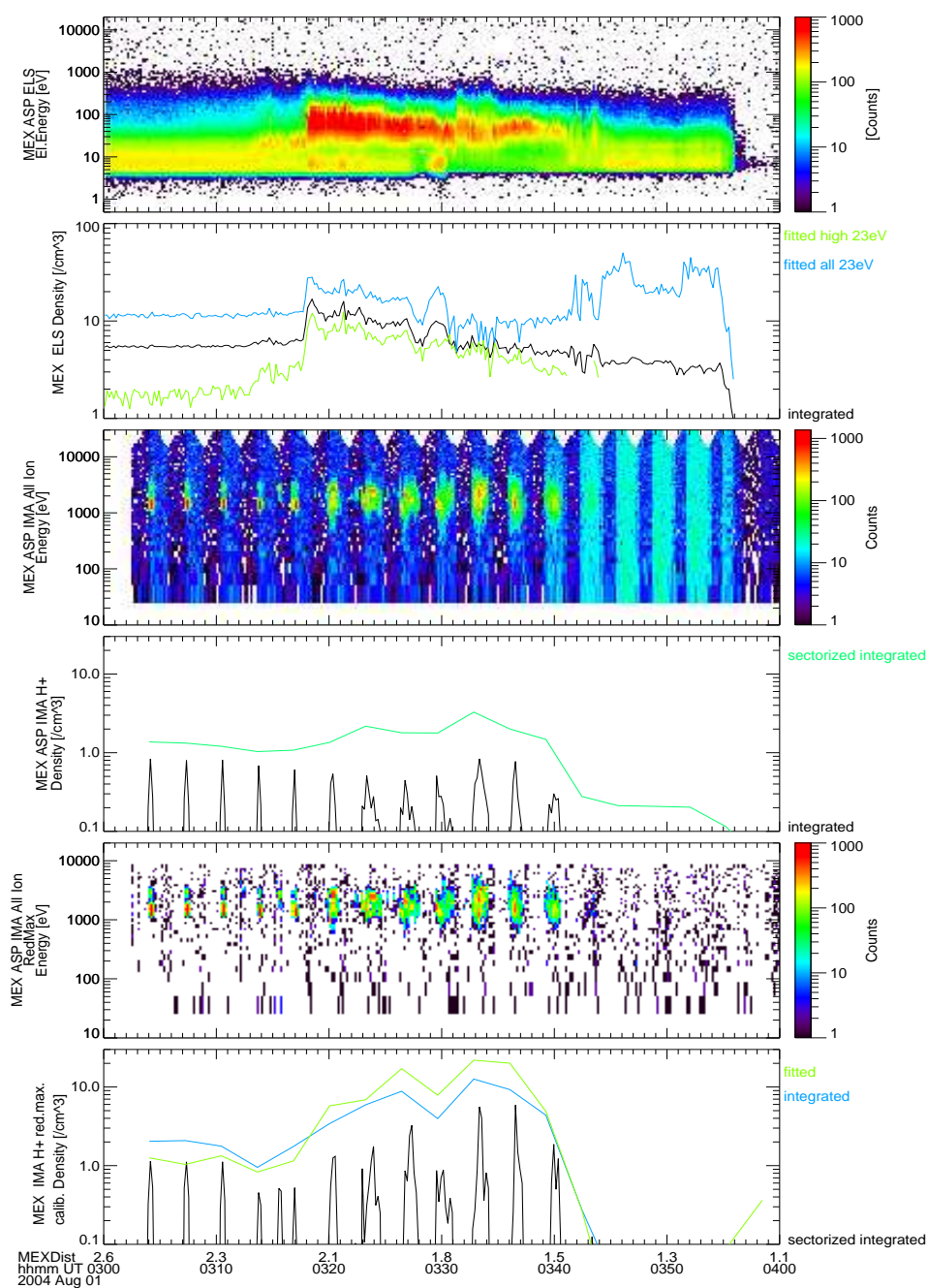


**Fig. 10** ASPERA-3 ELS and IMA data obtained between 2004-08-01 03:00 and 04:00UT. From top to bottom: a) uncalibrated ELS energy spectra, b) integrated and fitted ELS electron densities, c) non-reduced, uncalibrated IMA energy spectra, d) non-reduced integrated IMA  $H^+$  densities for each sector (black) and averaged over all sectors (green), e) reduced IMA energy spectrum f) reduced,calibrated IMA  $H^+$  densities for each sector (black), after calibration (blue) and fitted (green).

In the fifth panel of Fig.10 we apply noise reduction and calibration factors before calculating proton densities. Since here we take account of the sector efficiency we regard the integrated average density (blue line) as the best estimate for the proton density. If we remember that application of additional corrections for massring and anode efficiency might increase the intensity by a factor 2, agreement with the fitted high energy electron densities in solar wind and magnetosheath is rather good.

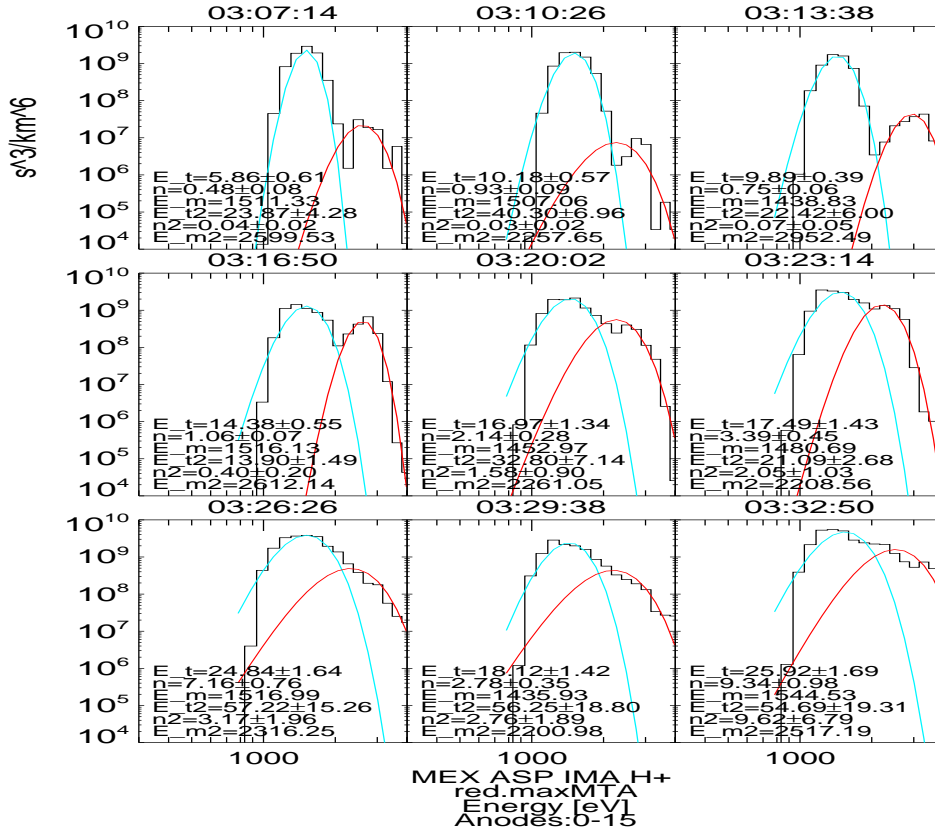


**Fig. 11** Phase space density of  $H^+$  as a function of energy, obtained by the ASPERA-3 IMA sensor in 2004-08-01 03:00UT to 03:30UT. Data are sampled over 192s. The black lines are the measured data, the blue lines are fits assuming a Gaussian distribution around the maximum of the spectrum. The red lines are a Gaussian fit to the high energy part of the spectrum. Fit parameters  $n$  [ $1/cm^3$ ],  $E_t$  [eV] and  $E_m$  [eV] are given for each fit.

Fig.11 shows fits to the IMA proton spectra for the first 30min of the time interval shown in Fig.10. The fit range is restricted to the 10 energy bins around the peak flux (blue fit). The energy bins above that range are fitted by a second Gaussian (red fit). The first four spectra are obtained in the solar wind. One can see that the fitted density is around  $1.0/cm^3$  indicating that the cold solar wind beam is probably slightly underestimated. One can also

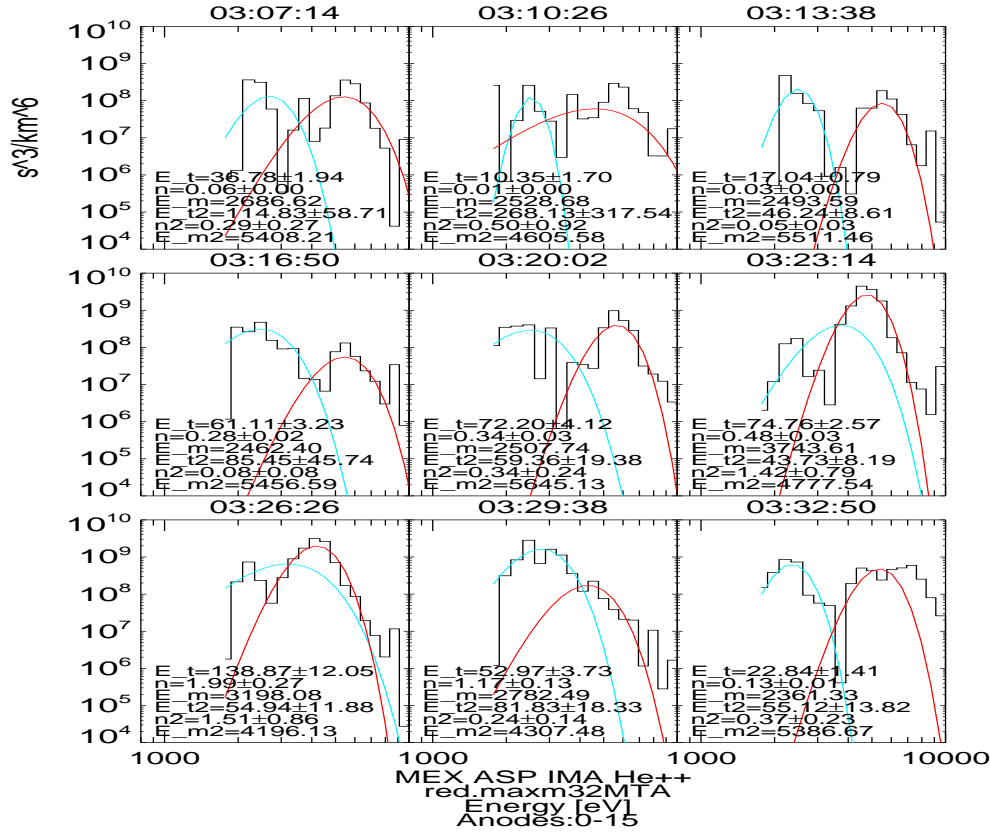


**Fig. 12** Phase space density of nominal He<sup>++</sup> as a function of energy, obtained by the ASPERA-3 IMA sensor in 2004-08-01 03:00UT to 03:30UT. Data are sampled over 192s. The black lines are the measured data, the blue lines are fits assuming a Gaussian distribution around low energy part of the spectrum. The red lines are a Gaussian fit to the high energy part of the spectrum. Fit parameters  $n$  [1/cm<sup>3</sup>],  $E_t$  [eV] and  $E_m$  [eV] are given for each fit.

observe a high energy component which increases when approaching the magnetosheath. The bimodal distribution observed after 03:13 is not well fitted by one gaussian, only the heated distributions after 03:26 are fitted well and give densities in agreement with calculation by integration. After 03:42 in the ionosphere no fit is possible.

This figure also shows the effect of the energy cut-off of the instrument which is between 500 and 700 eV depending on PAC level. This corresponds to bulk speeds of 310 and 370km/s respectively but distributions with higher bulk speeds are also affected such that we can say that only distributions with bulk speeds above 400km/s can be properly measured.

Fig.12 shows fits to the IMA He<sup>++</sup> spectra for the same time interval. These spectra have been obtained after proton spill-over subtraction. We expect the peak-energy to be four times the proton peak energy (the instrument measures E/Q, here the instrumental E/Q has been multiplied by 2). For the solar wind spectra that should be at about 5-7keV where a

high energy peak is actually observed. We interpret the peak at low energies as a residual of proton spill-over. Also the temperature of the  $\text{He}^{++}$ -peak in the cold solar wind seems to be over-estimated by the fit.

### 5.5.2 Ion Velocities

Fig.13 shows plasma velocity and temperature determinations by ELS and IMA for the same time interval as Fig.10. The two top panels show the energy spectra for reference. The next two panels show IMA proton and  $\text{He}^{++}$  velocity components determined by integration after calibration. The fifth panel from top shows the  $\vartheta$  and  $\varphi$  components of the proton velocity in the instrumental (ASP) system: whenever  $ABS(\varphi) > 90^\circ$  and  $\vartheta > 90^\circ$  the ion distribution might be partly shadowed by the spacecraft (the  $90^\circ$  line is shown in red for reference). We observe that in the solar wind (before 03:18 UT) both ions show  $V_x \sim -500$ ,  $V_z = 0$ ,  $V_y \sim -100$  km/s. In the magnetosheath the  $V_z$  components agree, while  $V_y$  and  $V_x$  do not. Specifically the  $\text{He}^{++}$  total velocity decreases while the proton velocity stays constant. We interpret this as an effect of the low energy cut-off of the proton distribution. That means, the  $\text{He}^{++}$ -velocity is usually a better measure of the ion speed but with the draw back of lower statistics. Note also, that after 03:27UT the velocity components in the ASP frame indicate that the distribution might be affected by shadowing. We do not show ELS electron velocities in this paper since the ELS measurements are planar and can only qualitatively represent the plasma velocity.

### 5.5.3 Temperature and Pressure

The lowest three panels of Fig.13 show electron and proton thermal pressures and temperatures. The third panel from bottom shows the electron temperature by integration (black), low-energy fitting (blue) and high-energy fitting (green). We assume that for the solar wind and magnetosheath integration and low-energy fitting deliver most of the times the temperature of spacecraft photo electrons only. Only in the ionosphere (after 03:42UT) - when the spacecraft potential is negative - these measures might be reasonable. But, it should be noted that also here distributions with temperatures of less than 1eV cannot be measured due to the shift in the spectrum caused by the negative spacecraft potential and the repellent voltage of ELS. The high-energy fitted temperature of  $\sim 15\text{eV}$  in the solar wind and 20-40eV in the sheath are the better measure in these regions and in agreement with the fitted proton temperature. The bottom panel of Fig. 13 shows solar wind electron and proton pressures in the range 1-5 pPa, magnetosheath electron pressures of 10-30 pPa, and proton pressures of 80-200 pPa.

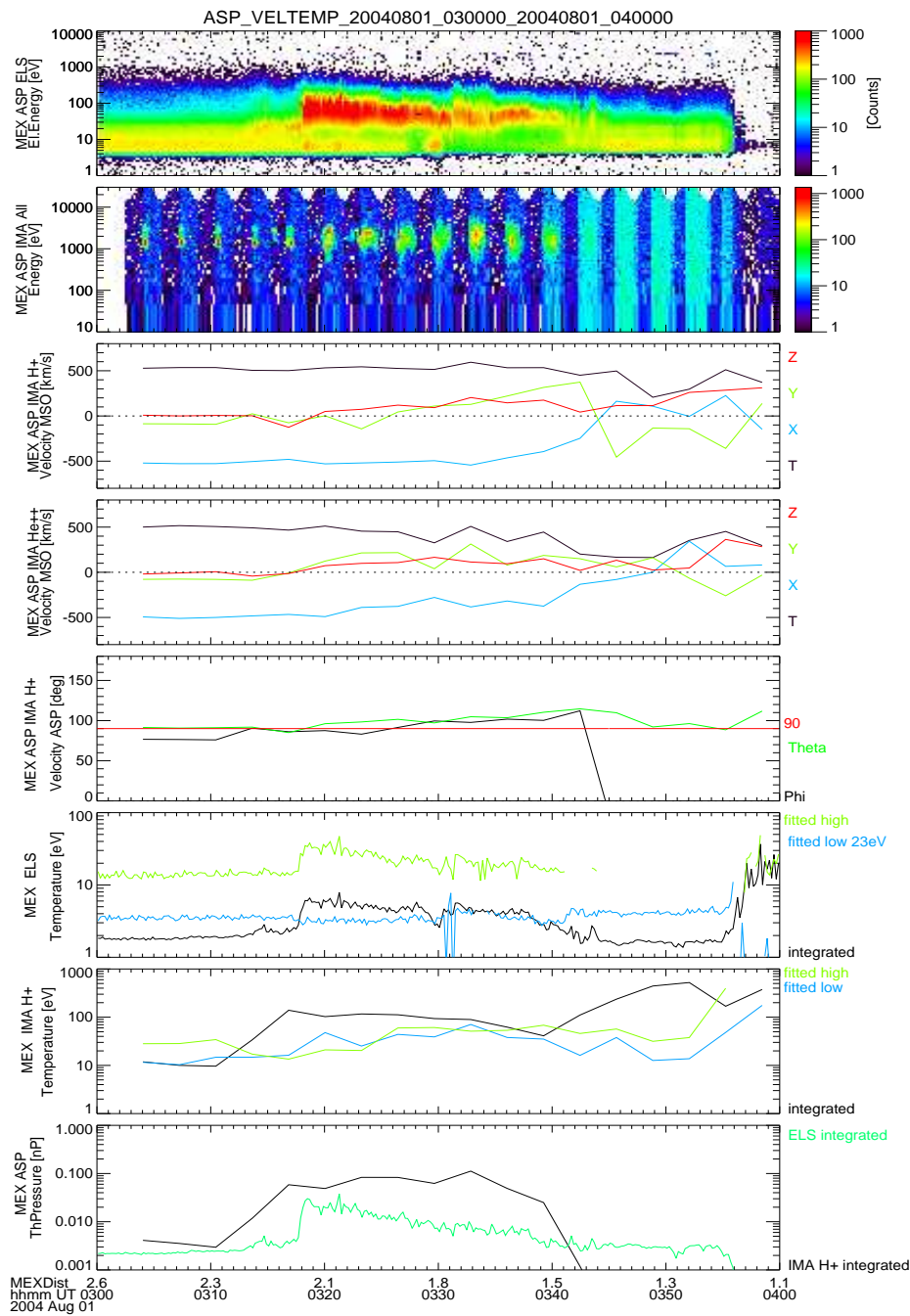


**Fig. 13** ASPERA-3 ELS and IMA data obtained between 2004-08-01 03:00 and 04:00UT. From top to bottom: a) ELS electron energy spectrum, b) IMA all ion energy spectrum, c) IMA proton velocity with anode and sector calibration xyz and total components (MSO system), d) IMA He<sup>++</sup> velocity with anode and sector calibration xyz and total components (MSO system), e) IMA proton velocity ASP  $\vartheta$  and  $\varphi$  components, f) ELS electron temperatures by integration (black), fitting low energies (blue) and high energies (green). g) IMA proton temperatures by integration (black), fitting low energies (blue) and high energies (green). h) IMA total proton thermal pressure (black) and ELS total electron thermal pressure.

## 6 Plasma moment statistics in the environment of Mars

In the following we apply the moment calculations discussed in the previous sections to the complete ASPERA-3 ELS and IMA data sets obtained between 1 Feb 2004 and 1 Feb 2006 at full time resolution (4s for ELS and 192s for IMA). For ELS we exclude periods of linear stepping mode, for IMA we only use PAC level 1 and 2 data, exclude periods of spacecraft shading of the sensor by taking records with a bulk speed inside the core field-of-view of the sensor. Also we only use spectra where the integrated proton density is larger than  $0.1/\text{cm}^3$ . The last condition excludes most spectra obtained with IMA inside of the MPB where light ions are rarely observed.

As discussed in the beginning of this paper plasma moments can be obtained either by integration of the energy spectra or by fitting a Gaussian to the phase space distribution function. While the integration usually covers the complete energy spectrum, we fit low and high energy parts of the spectrum separately for distributions outside the ionosphere. The parameters discussed in the following are: 1. the low and high energy electron density by fitting, 2. the low and high energy electron temperature by fitting, 3. the proton density, velocity and temperature by fitting and integration, and 4. the alpha density by fitting and integration.

### 6.1 Spatial binning

In this paper we only discuss mean and maximum values of plasma moments sampled over the first two years of operation of Mars Express in orbit. We use the MEX orbital data in the Mars-Solar-Orbital system (MSO) where the positive X-axis is defined by the instantaneous Mars-Sun line and the Y-axis points against the Mars orbital velocity vector. The Z-axis then points approximately in ecliptic north direction. We calculate mean values by binning the data on a spatial grid where the X-axis is defined by the MSO X-axis and the Y-axis by  $R_{cyl} = \sqrt{Y_{MSO}^2 + Z_{MSO}^2}$ , that is we assume cylindrical symmetry with respect to the Mars-Sun line. We do not take account of aberration effects by the Mars orbital speed (24.1km/s), since it is low compared to the errors of measurement. Dawn-dusk or North-South asymmetries are usually related to the orientation of the interplanetary magnetic field. Since Mars Express does not have a magnetometer on board, the IMF orientation can only be estimated by using a proxy from MGS data. We are planning to bin the data according to IMF orientation in a later paper. The bin size we are using is 0.05 Martian radii or 170km for electrons and 0.1 Martian radii or 340km for ions. Since electrons are sampled at 4s per spectrum we get more than 100 samples/bin for most regions covered by the orbits (Fig.14 top). For ions the acquisition time is only 192s per full 3D spectrum such that we use a coarser grid and get between 10 and 100 samples per bin (Fig.14 bottom). In all figures black shaded bins denote a value which is equal or less than the minimum value of the color bar, red shaded bins denote values which are higher than the maximum value of the color bar. White space means that no valid samples were taken here. We use three different statistical measures to determine moment levels for each spatial bin: the median (value for which same number of samples have value above and below), the mean (sum over all samples divided by number of samples) and the maximum value observed during the measurement interval 1 Feb 2004 to 1 Feb 2006. Since data of particle counters are typically influenced by disturbances which may only show up sporadically - like solar UV-light on the sensors, there are outliers in the data which can falsify the maximum values observed but also the mean values. Thus the median is usually the most robust measure of the average of the data.

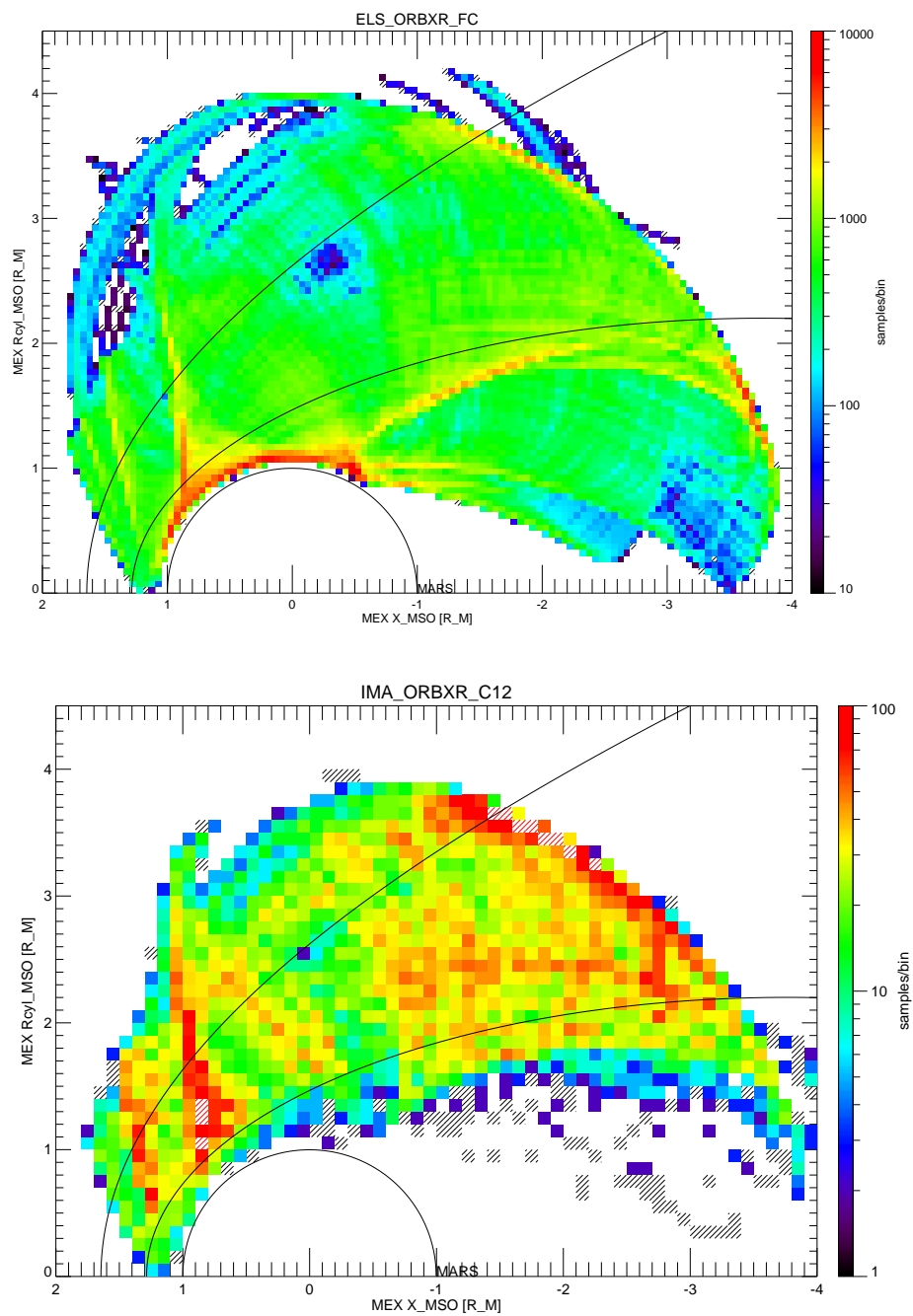


**Fig. 14** Number of data samples per bin obtained by the ELS sensor in logarithmic stepping mode (top) and the IMA sensor for PAC level 1 and 2 with  $n_p > 0.1/\text{cm}^3$  between 01 Feb 2004 and 01 Feb 2006 binned on an MSO X-Rcy1 grid with a gridsize of 0.05 and 0.1  $R_M$  respectively.

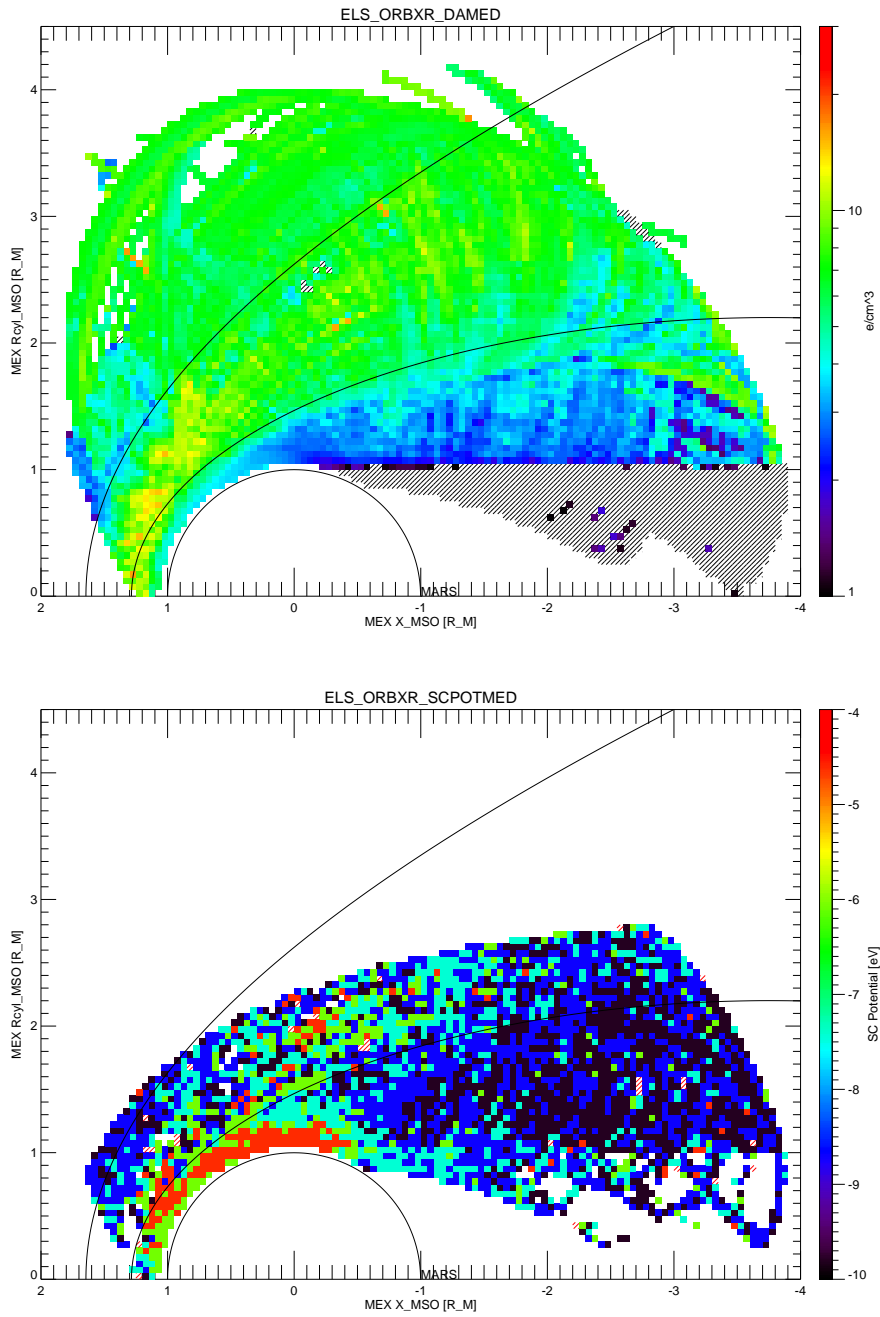


**Fig. 15** Median integrated electron density over all energies (top) and median ionospheric spacecraft potential estimate (bottom) assuming  $CO_2$  peaks at 23eV. Observations by the ELS sensor between 01 Feb 2004 and 01 Feb 2006 binned on an MSO X-Rcyl grid with a gridsize of  $0.05 R_M$ .

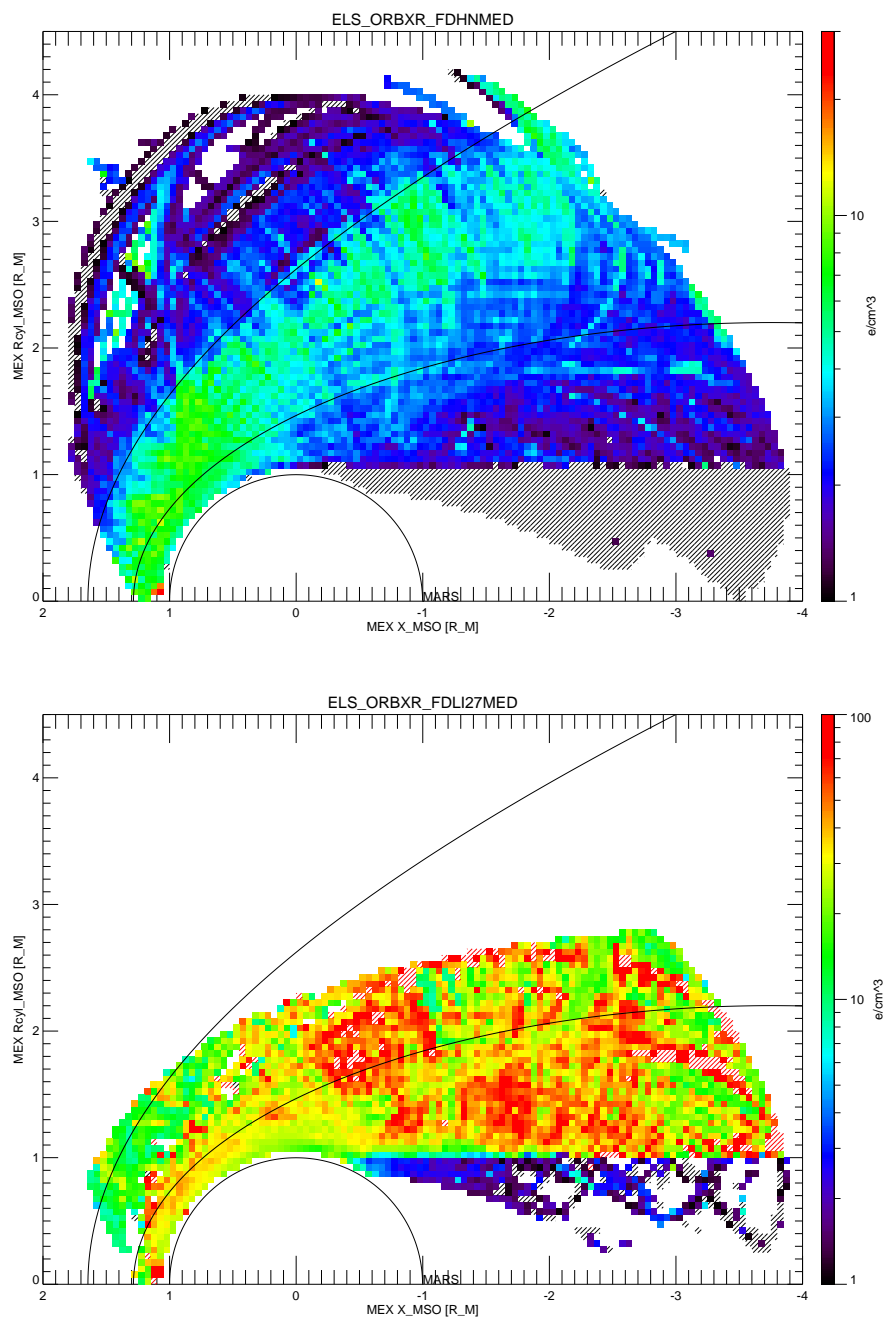


**Fig. 16** Median of fitted high-energy electron density for non-ionospheric spectra (top) and low-energy electron density for ionospheric spectra (bottom) observed by the ELS sensor between 01 Feb 2004 and 01 Feb 2006 binned on an MSO X-Rcy1 grid with a gridsize of  $0.05 R_M$ .

## 6.2 Electron densities

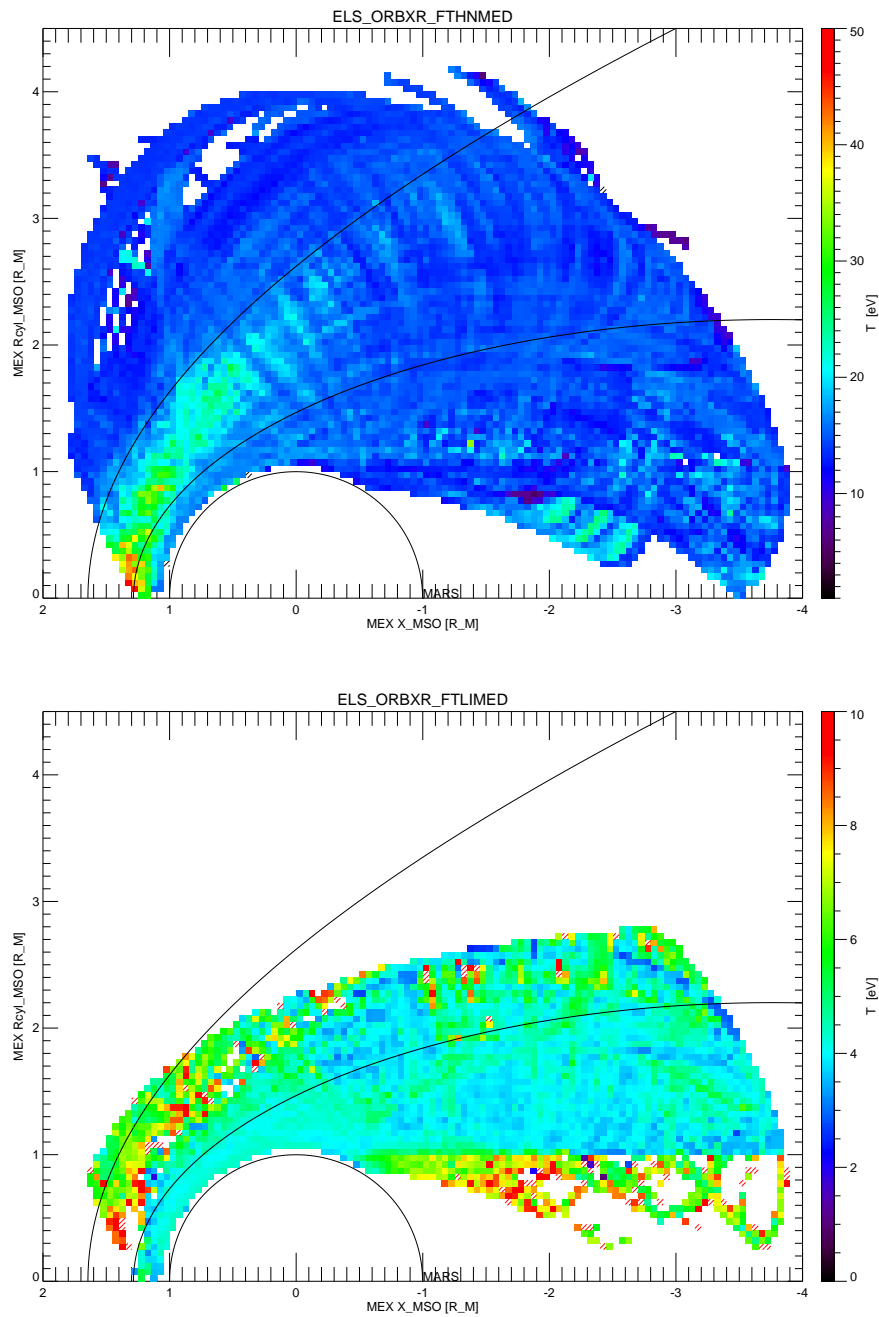
As discussed in the first part of this paper it is a general problem of electron counters flying in space that electrons of energies with less than about 10eV are not registered by the instrument when the spacecraft potential is negative or overenhanced when the spacecraft potential is positive. In addition electrons with less than 5eV are reflected by the an additional grid to avoid counter saturation. For ionospheric spectra the energy resolution of the ELS sensor of the ASPERA-3 experiment is good enough to observe the non-thermalized photo-electron peaks expected in the energy range 20-30eV. The location of these peaks allows one to estimate the spacecraft potential and subsequently we extrapolate the spectrum to energies below 10eV. For non-ionospheric spectra we do not have an indication of the spacecraft potential and can only extrapolate the low energies assuming fixed values of the potential. Note, that the energy determining geometric factors and efficiency of each energy channel is the actually measured energy while the energy shift by spacecraft potential is applied after applying these factors. Thus the effect of the shift on the efficiency is covered.

Fig.15 top shows the median electron density calculated by integration with spacecraft potential correction. Here the spacecraft potential has been estimated as +5V for non-ionospheric spectra and calculated assuming photo electron peak energy at 23eV. The separation method for ionospheric and non-ionospheric spectra has been discussed in section 4.1. A respective map of the resulting ionospheric spacecraft potentials is shown as Fig.15 bottom. Note, that potential values are determined for each 4s spectral value separately depending on the closest observation of a photoelectron peak. Since the spacecraft potential is being determined whenever a 4s spectrum is classified ionospheric by the ratio of low energy to high energy counts, this map also shows that this criterion is fulfilled by some spectra in the magnetosheath and solar wind. To reduce this effect we impose the additional criterion for ionospheric spectra that the point of measurement must be not more than 0.5 Martian radii away from the MGS MPB and that the closest observed CO<sub>2</sub> peak must not be more than 10min away in measurement time.

In solar wind, sheath and ionosphere the integrated density gives a wrong measure of the actual density - only in the magnetotail with sparse distributions it can be assumed a better measure than the fitted values. We show the map here mainly as a guide to the actual measured counts. Overplotted as black lines on all figures are the bowshock and MPB location as observed by the MGS magnetometer[19].

In Fig.16 top we show median fitted densities calculated from the high energy part of the spectrum only. Here we observe densities of 1-3/cm<sup>3</sup> for the solar wind, which agrees with the proton observations (see below). For the magnetosheath the same influence of spacecraft photoelectrons prevails such that here also Fig.16 top gives the best density estimate very much in agreement with proton density observations. We also observe that the presumed positive spacecraft potential value does only have a minor influence on solar wind and magnetosheath densities. Fig.16 bottom shows the median fitted low-energy electron density for ionospheric spectra. We regard the high density values observed for zenith angles larger than 100 degree as artefacts of an erroneous spacecraft potential estimation or bad fitting by low counting statistics.

For the ionosphere the determination of electron densities is much more problematic. The minimum altitudes reached by Mars Express is about 260km. Electron densities for altitudes below 300km have been determined on previous missions by radar sounding and radio occultation [10]. While maximum densities of 10<sup>5</sup>/cm<sup>3</sup> are reported below 200km altitude, for solar zenith angles below 45 degree densities fall to 10<sup>3</sup>/cm<sup>3</sup> at 300km altitude. The median densities we observe for the lowest MEX altitudes are only 20-40/cm<sup>3</sup> when



**Fig. 17** Median of fitted high-energy electron temperature for non-ionospheric spectra (top) and of fitted low-energy electron temperature for ionospheric spectra (bottom) observed by the ELS sensor between 01 Feb 2004 and 01 Feb 2006 binned on an MSO X-RcyL grid with a gridsize of  $0.05 R_M$ .

assuming a 23eV photoelectron peak (not shown here) or 40-70/cm<sup>3</sup> when assuming a 27eV photoelectron peak (Fig.16 bottom). A more detailed comparison of ionospheric densities with radio sounding results of the MARSIS experiment on Mars Express has to be done to resolve this issue.

### 6.3 Electron temperatures

Fig.17 top shows the median electron temperature for the high-energy part of the spectrum and non-ionospheric spectra. In the solar wind we observe temperatures of 10-20eV which is higher than the expected 1-5eV [18]. This might be an artefact of a bad separation of the high-energy tail of the spectrum in the solar wind. Towards the bow shock the temperature seems to increase which might be an effect of upstreaming electrons or just the fluctuation of the bow-shock position. In the magnetosheath we think that as for the densities the high-energy part of the spectrum (Fig.17 bottom) will give the better estimate. Here we observe temperatures of 20-40eV for zenith angles smaller than 90 degree and slightly lower for larger angles. For the ionosphere only the low-energy part (Fig.17 bottom) is relevant and the map seems to indicate that temperatures decrease with altitude at solar zenith angles smaller than 90 degree. But minimum temperatures in the ionosphere are about 4eV. Hanson and Mantas[7] give temperatures of only 0.5eV for 300km altitude. While the ELS sensor has an energy resolution sufficient to measure such low energies, we think that in a region of negative spacecraft potential  $P$  the minimum temperature which can be measured is given by  $eP$ , which is about 4eV.

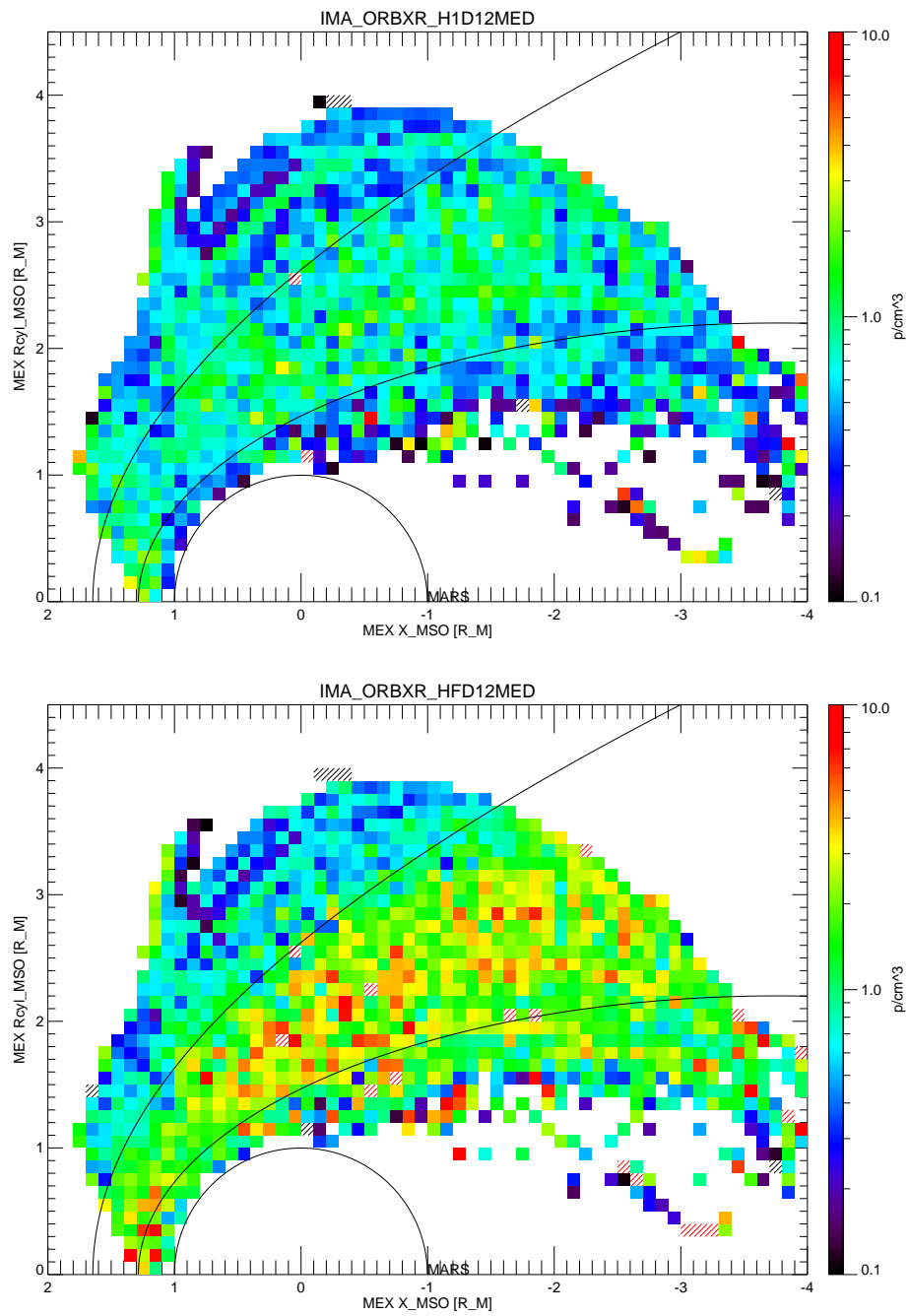
### 6.4 Proton densities

Fig.18 shows median proton densities obtained by integrating and fitting the spectra of the IMA sensor. We observe typical proton densities of about 1/cm<sup>3</sup> outside of the bow-shock and 1-3/cm<sup>3</sup> by integration and 3-5/cm<sup>3</sup> by fitting in the magnetosheath. This difference is probably caused by the instrumental cut-off below 1keV which is better extrapolated by the fitting. The fitted values agree with observations by the ASPERA-1 experiment on Phobos-2 [12]. At the MPB densities drop well below 1/cm<sup>3</sup>. The median fall-off location of the proton density seems also to agree with the MGS MPB.

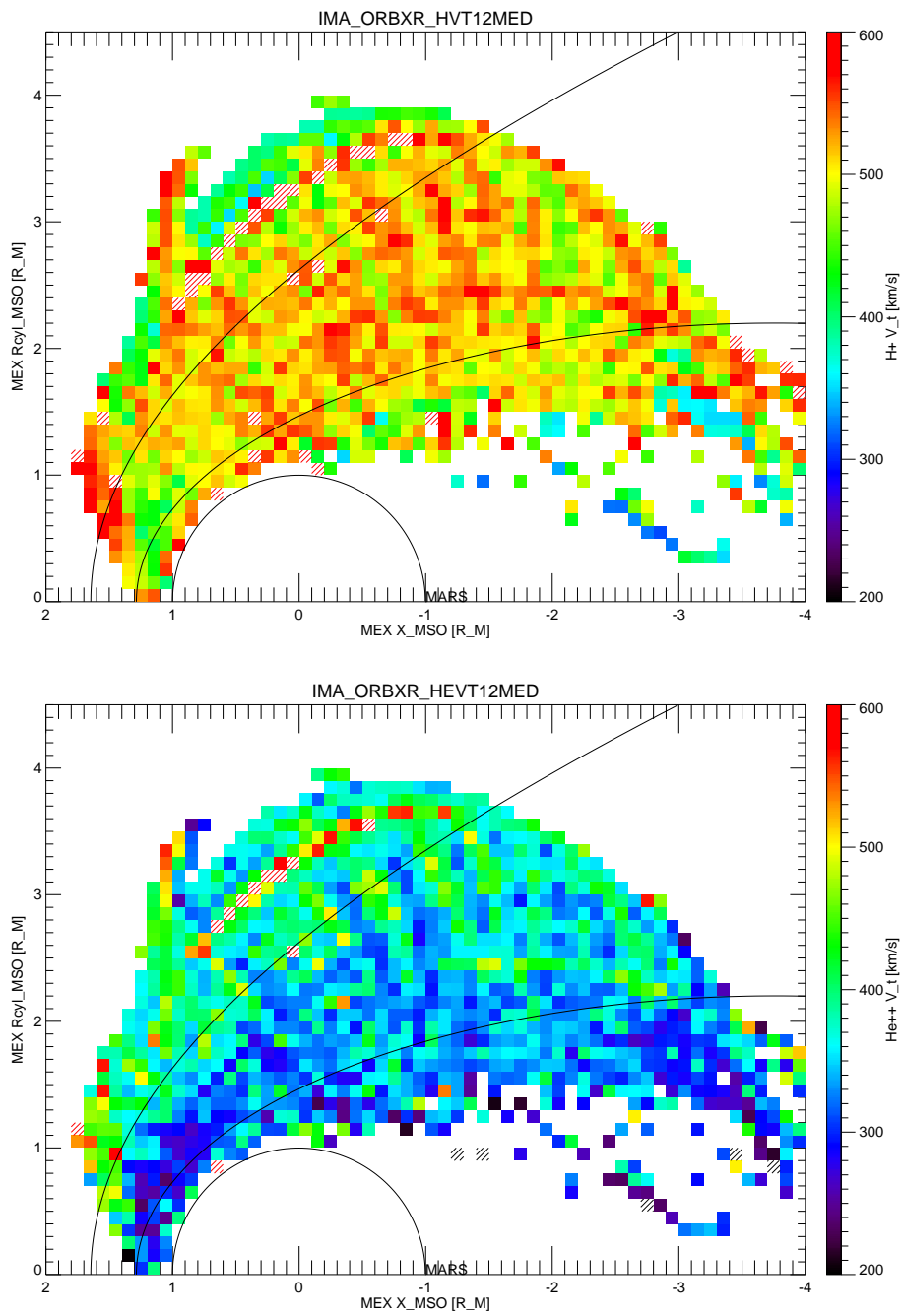
### 6.5 Ion Velocities

Fig.19top shows the total proton velocity observed by the IMA sensor at typical median values of 500km/s in solar wind and magnetosheath. Because of the low-energy cut-off of the sensor there is a strong bias towards high velocities in the proton data. As estimated above (section 5.5.1) only distributions with bulk speeds over 400km/s are correctly sampled. A better estimate is the He<sup>++</sup>-velocity shown in Fig.19bottom. Here we observe a more reasonable median solar wind speed of 300-400km/s and braking of the speed by about 50km/s at the bow shock.

Fig.20 shows the median velocity vector orientation in MSO cylindrical coordinates for protons (top) and He<sup>++</sup>(bottom). Here we can observe nicely the deviation of the solar wind by the obstacle: in the inner magnetosheath at solar zenith angles of 45 to 90 degrees vectors are almost parallel to the MGS MPB. Since the velocity vector orientation does not depend



**Fig. 18** Median of integrated (top) and fitted (bottom) proton density observed by the IMA sensor in PAC 1 and 2 between 01 Feb 2004 and 01 Feb 2006 binned on an MSO X-RcyL grid with a gridsize of  $0.1 R_M$ .



**Fig. 19** Median of integrated total proton velocity (top) and of integrated total He<sup>++</sup> velocity (bottom) observed by the IMA sensor in PAC 1 and 2 between 01 Feb 2004 and 01 Feb 2006 binned on an MSO X-RcyL grid with a gridsize of  $0.1 R_M$ .

strongly on the energy range, there are only small differences between proton and He++ observations.

## 6.6 Proton Temperatures

Fig.21 shows the median proton temperature calculated by integration (top) and by fitting (bottom). The fit here includes the low and high energy part of the spectrum. For the temperature the two methods show very different values: integrated temperatures are at around 100eV and above in the magnetosheath, while fitted values are at about 10-30eV in the solar wind and 30-50eV in the sheath. The fitted values agree with expected values for the solar wind [18] which indicates that the high temperatures calculated by integration might be caused by high energy noise or by the bad spatial resolution of the IMA sensor. For the magnetosheath the bad spatial resolution is much less important. The fitting of proton spectra is done only for limited energy ranges (see section 5.5). This limits the maximum temperatures which can be fitted. Thus we may assume that for the magnetosheath the integrated values may be more representative since they also show maximum temperatures at the nose as one would expect. On the other hand the integrated temperature is more influenced by the low-energy cut-off than the fitted values. Here the ASPERA-1 experiment also reported very high values of around 600eV [12], which is much higher than our median values.

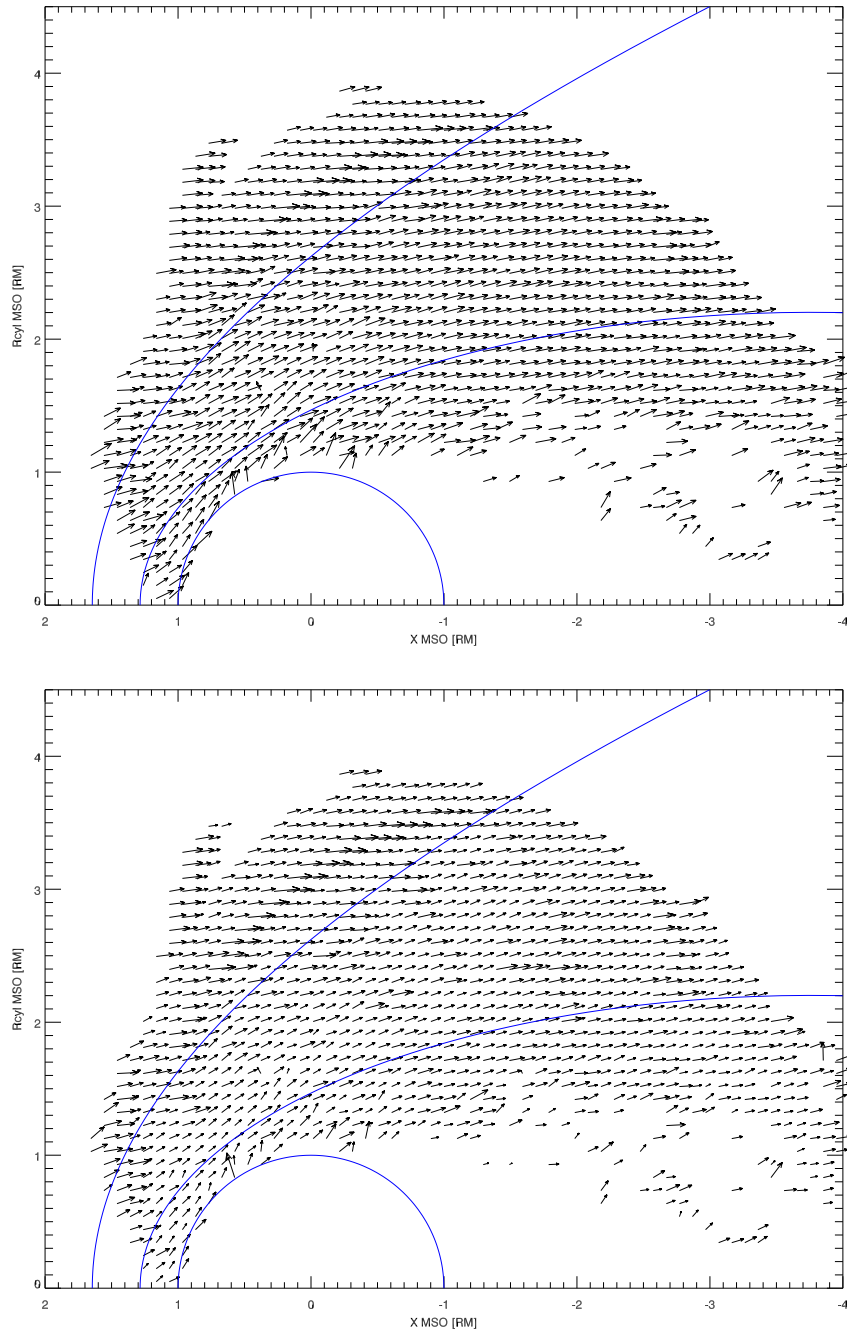
## 6.7 Alpha densities

Fig.22 shows the integrated and fitted alpha particle densities observed by the IMA sensor. Here we calculated the densities over the complete energy range. As discussed in section 5.5 this might overestimate the densities since at lower energies the alpha track is contaminated by spill-over protons. Still the observed values are on the order of 0.2-0.3/cm<sup>3</sup> which is about 10% of the proton densities. Fitted values show much better the density increase at the bow shock.

## 7 Summary and Conclusions

In the first part of this paper we have presented methods to derive plasma moments from the ion sensors of the ASPERA-3 experiment onboard Mars Express. This is the first time that plasma moments have been determined in a wide range of conditions in the environment of Mars. After two years of operation of the ASPERA-3 instrument we are still learning about the instruments behavior under changing conditions. Thus we expect that certain calibration parameters and interpretations will change in the coming years of ASPERA data analysis. But we expect that the principles described in this paper remain valid and that the derived moments will not change dramatically. The values we derive for density, temperature and velocity of electrons and protons are very reasonable when the spacecraft crosses solar wind and magnetosheath regions. For the ionosphere we have the specific problem of very low energy electron and ion distributions. Only further comparisons with other instruments (MARSIS) will show how good our determinations are for this region.

Each ion species has its specific problems for the moment calculation: for electrons we have the influence of the spacecraft potential and local photo electrons. In addition the planar measurement without a magnetometer onboard prohibits the determination of the electron



**Fig. 20** Median of integrated proton velocity (top) and He++ velocity (bottom) vector orientation in the MSO system observed by the IMA sensor in PAC 1 and 2 between 01 Feb 2004 and 01 Feb 2006 binned on an MSO X-RCyl grid with a gridsize of  $0.1 R_M$ .

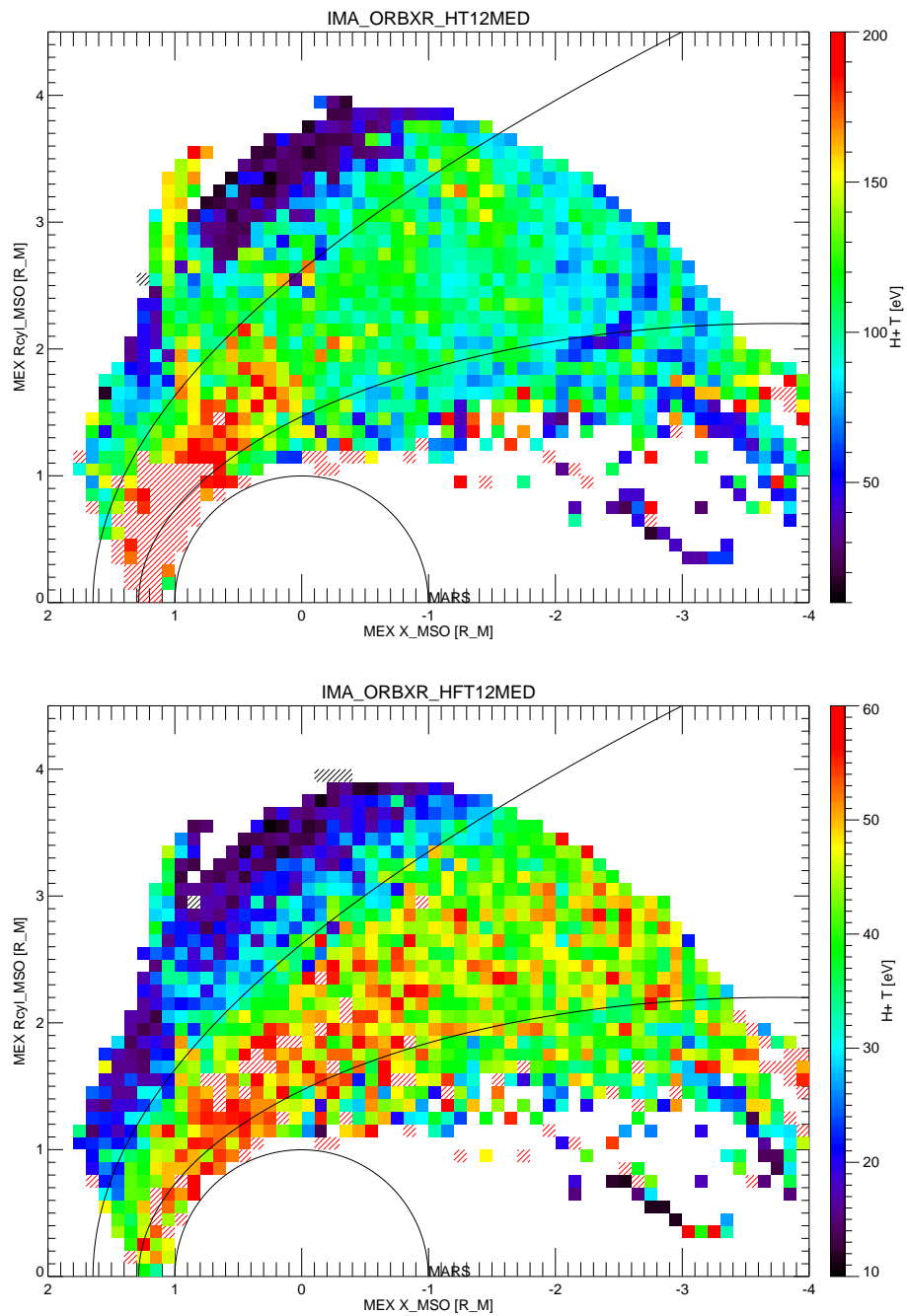


**Fig. 21** Median of integrated (top) and fitted (bottom) proton temperature observed by the IMA sensor in PAC 1 and 2 between 01 Feb 2004 and 01 Feb 2006 binned on an MSO X-RcyL grid with a gridsize of 0.1  $R_M$ .

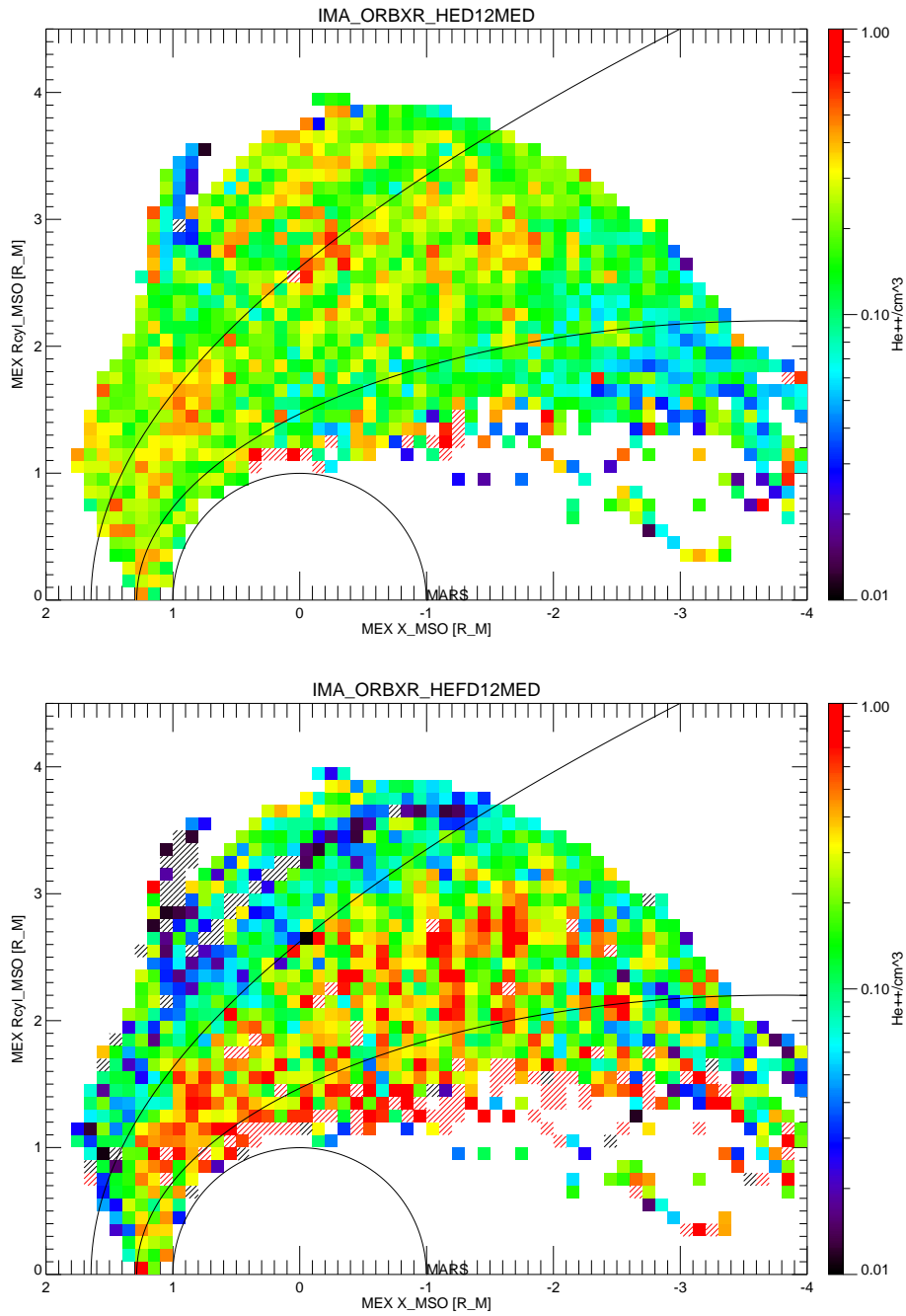


**Fig. 22** Median of integrated (top) and fitted (bottom) alpha particle density observed by the IMA sensor in PAC 1 and 2 between 01 Feb 2004 and 01 Feb 2006 binned on an MSO X-RcyL grid with a gridsize of 0.1  $R_M$ .

velocity vector. For protons we have the problem of an energy cut-off at about 500eV in addition to the high noise level of the instrument. For helium and heavier ions we have the problem of spill-over protons - that is protons which are erroneously registered with a high mass/charge value. Nevertheless we think that we have shown in this paper that we can derive moments which are consistent in very different plasma conditions.

In the second part of this paper we have been presenting the first maps of plasma moments for the space environment of Mars obtained by the ASPERA-3 experiment on board Mars Express. These moments include densities and temperatures for electrons and protons, densities for alpha particles and velocities for protons. Proton and alpha moments are strictly valid for solar wind and the magnetosheath only because of the low energy cut-off of the instrument. Moments of heavier ions will be treated in a later paper. We observe median density values of  $2\text{-}3/\text{cm}^3$  and proton temperatures of 20-30eV in the solar wind as expected for solar distances of 1.5AU. In the magnetosheath densities increase by a factor 2-3 and ion temperatures by a factor 2. Recently these values have been compared with a 3D hybrid simulation of the Martian plasma environment [2]. The results showed qualitative agreement for most parameters and quantitative agreement for electron and proton densities and temperatures.

We think that using the correction by spacecraft potential we are even able to estimate ionospheric electron moments, which is difficult when using particle counters with a low energy cut-off. Also the spatial binning used for this paper is too coarse to determine densities at lowest altitudes. Still the maximum values observed at 300km altitude indicate that densities reach up to  $10^3/\text{cm}^3$  in agreement with radio occultation observations. To resolve the long-standing question whether the ionospheric particle pressure is sufficient to balance the solar wind pressure, we need additional investigations using the heavy ion data of ASPERA-3.

**Acknowledgements** We thank all members of the ASPERA-3 team for the big effort which led to the successful operation of the instrument and the calibration of the data. For this paper we are especially grateful to Emmanuel Penou, CESR, for data preparation. We wish to acknowledge support from DLR grant 50QM99035 and Deutsche Forschungsgemeinschaft grant WO 910/1-1, support through the National Aeronautics and Space Administration (NASA) contract NASW-00003 in the United States, and the Particle Physics and Astronomy Research Council (PPARC) in the United Kingdom.

## References

1. Barabash, S., Lundin, R., Andersson, H., Gimholt, J., Holmström, M., Norberg, O., Yamauchi, M., Asamura, K., Coates, A.J., D.R.Linder, D.O.Kataria, Curtis, C.C., Hsieh, K.C., Fedorov, B.R.S.A., Grigoriev, A., Budnik, E., Grande, M., Carter, M., Reading, D.H., Koskinen, H., Kallio, E., Riihela, P., SÅ¶les, T., Kozyra, J., Krupp, N., Livi, S., Woch, J., Luhmann, J., McKenna-Lawlor, S., Orsini, S., Cerulli-Irelli, R., Mura, A., Roelof, A.M.E., Williams, D., Sauvaud, J.A., Winningham, J.J.T.D., Frahm, R., Scherrer, J., Wurz, J.S.P., Bochsler, P.: The analyzer of space plasmas and energetic atoms (ASPERA-3) for the European Mars Express mission. *Space Sci.Rev.* **this issue** (2006)
2. Bößwetter, A., Simon, S., Bagdonat, T., Motschmann, U., Fränz, M., Roussos, E., Krupp, N., Woch, J., Schüle, J., Barabash, S., Lundin, R.: Comparison of plasma data from aspera-3/mars-express with a 3d hybrid simulation. *Ann.Geophys.* **submitted** (2006)
3. Brain, D., Bagenal, F., Acuña, M., Connerney, J.: Martian magnetic morphology: Contributions from the solar wind and crust. *J.Geophys.Res.* **108**(A12), doi:10.1029/2002JA009482 (2003)
4. Carlsson, E., Fedorov, A., et al.: Mass composition of escaping plasma at Mars. *Icarus* **182**(2), 320–328 (2006)
5. Dubinin, E., Fraenz, M., Woch, J., Barabash, S., Lundin, R., Yamauchi, M.: Hydrogen exosphere at mars. pickup protons and their acceleration at the bow shock. *Geophys.Res.Lett.* **submitted** (2006)
6. Frahm, R., Winningham, J., et al.: Carbon dioxide photoelectron peaks at mars. *Icarus* **182**(2), 371–382 (2006)

- 
7. Hanson, W., Mantas, G.: Viking electron temperature measurements: evidence for a magnetic field in the Martian ionosphere. *J.Geophys.Res.* **93**, 7538 (1988)
  8. Hutchinson, I.: Principles of plasma diagnostics, 2nd edition. Cambridge University Press, Cambridge, UK (2002)
  9. Kallenrode, M.B.: Space physics: An introduction to plasmas and particles in the Heliosphere and magnetospheres. Springer, Berlin, Germany (1998)
  10. Kliore, A.: Radio occultation observations of the ionospheres of Mars and Venus. *AGU Geophys.Monograph* **66**, 265 (1992)
  11. Luhmann, J., Brace, L.: Near-Mars space. *Rev.Geophys.* **29**(2), 121–140 (1991)
  12. Lundin, R., et al.: ASPERA Observations of Martian Magnetospheric Boundaries in Plasma environment of non-magnetic planets (T.Gombosi, Edt), pp. 311–320. Pergamon (1993)
  13. Mantas, G., Hanson, W.: Photoelectron fluxes in the Martian ionosphere. *J.Geophys.Res.* **84**, 369–385 (1979)
  14. Mazelle, C., Winterhalter, D., Sauer, K., Trotignon, J., Acuña, M., Baumgartel, K., Bertucci, C., Brain, D., Brecht, S., Delva, M., Dubinin, E., Oieroset, M., Slavin, J.: Bow shock and upstream phenomena at Mars. *Space Sci.Rev.* **111**(1-2), 115–181 (2004)
  15. Nagy, A., Winterhalter, D., Sauer, K., Cravens, T., Brecht, S., Mazelle, C., Crider, D., Kallio, E., Zakharov, A., Dubinin, E., Verigin, M., Kotova, G., Axford, W., Bertucci, C., Trotignon, J.: The plasma environment of Mars. *Space Sci.Rev.* **111**(1-2), 33–114 (2004)
  16. Parks, G.: Physics of Space Plasmas: An Introduction. Perseus, Cambridge, Mass. (1991)
  17. Paschmann, G., Fazakerley, A., Schwartz, S.: Moments of Plasma Velocity Distributions, in: Analysis Methods for Multi-Spacecraft Data. ISSI/ESA, Bern, CH (2000)
  18. Schwenn, R.: Large-Scale Structure of the Interplanetary Medium in Physics of the inner heliosphere, vol. 1, chap. 3. Springer (1991)
  19. Vignes, D., Mazelle, C., Rème, H., Acuña, M., Connerney, J., Lin, R., Mitchell, D., Cloutier, P., Crider, D., Ness, N.: The solar wind interaction with Mars: locations and shapes of the bow shock and the magnetic pile-up boundary from the observations of the MAG/ER experiment onboard Mars Global Surveyor. *Geophys.Res.Lett.* **27**(1), 49–52 (2000)